Rotating fluid cylinder
subject to weak precession

By PATRICE MEUNIER[1], CHRISTOPHE ELOY[1],
ROMAIN LAGRANGE[1] AND FRANÇOIS NADAL[2]

[1]IRPHE, CNRS, Universités Aix Marseille I & II, 49 rue Joliot–Curie, 13013 Marseille, France
[2]Commissariat à l'Energie Atomique, CESTA, 33114 le Barp, France

In this paper, we report experimental and theoretical results on the flow inside a precessing and rotating cylinder. Particle Image Velocimetry measurements have revealed the instantaneous structure of the flow and confirmed that it is the sum of forced inertial (Kelvin) modes, as predicted by the classical linear inviscid theory. But this theory predicts also that the amplitude of a mode diverges when its natural frequency equals the precession frequency. A viscous and weakly nonlinear theory has therefore been developed at the resonance. This theory has been compared to the experimental results and shows a good quantitative agreement. For low Reynolds numbers, the mode amplitude scales as the square root of the Reynolds number due to the presence of Ekman layers on the cylinder walls. When the Reynolds number is increased, the amplitude saturates at a value which scales as the precession angle power one third for a given resonance. The nonlinear theory also predicts the forcing of a geostrophic (axisymmetric) mode which has been observed and measured in the experiments. These results allow to fully characterise the flow inside a precessing cylinder in all regimes as long as there is no instability.

1. Introduction

In the field of aerospace, the stability of spinning spacecrafts containing propellant liquids is still a topical question. For instance, the attitude of spinning satellites (see Stewartson 1958; Gans 1984; Garg *et al.* 1986; Agrawal 1993; Bao & Pascal 1997) is likely to be disrupted by the hydrodynamics of the inside fluid. Consequently, a good understanding of the behaviour of such a fluid–structure coupled system requires a precise knowledge of the dynamics of the rotating contained fluid. Moreover, rotating fluid dynamics lies far beyond the scope of aerospace : a lot of atmospheric phenomena (hurricanes, tornadoes), are closely connected to this class of problems, due to the predominant role played by the Coriolis force at low Rossby numbers (Vanyo 1993).

First experimental and theoretical studies on rotating fluids date from the end of the 19th century. Lord Kelvin (1880) suggested that the flow of a disturbed rotating fluid could be decomposed into a sum of so-called normal Kelvin modes (i.e. inertia waves), each of them corresponding to a well defined frequency which is always less than twice the basic rotation frequency. The inviscid approach of Kelvin can be extended in the limit of large Reynolds numbers by taking into account viscous boundary layers on the walls of the container as shown by Kudlick (1966) and Greenspan (1968). A large set of experimental and numerical studies in the case of a completely filled cylinder (see Fultz

1959; McEwan 1970; Kobine 1995; Kerswell & Barenghi 1995) has confirmed the values of the frequencies and viscous decay rates predicted by these theories.

An important aspect of these rotating flows is that Kelvin modes have been shown to become unstable for large Reynolds numbers. McEwan (1970) first showed that when a rotating fluid cylinder is forced at a given frequency on one of its ends, Kelvin modes are forced. One of these Kelvin modes can become resonant if its wavelength matches the height of the cylinder. This leads to a *resonant collapse* (i.e. a breakdown of the initial mode) degenerating into a fine-scale disordered flow. In some cases, this very disordered flow can relaminarise into solid body rotation again leading to a cycle of instability, breakdown and relaminarisation. These behaviours have also been reported when the Kelvin modes are forced in a partly filled and tilted cylinder (Thompson 1970) or in completely filled cylinder in precession (Manasseh 1992; Mahalov 1993) or when they are the natural modes of an instability such as the elliptic instability (Malkus 1989; Eloy *et al.* 2000; Kerswell 2002; Eloy *et al.* 2003). The physical mechanism leading to the breakdown is still unclear but several scenarios have been proposed. Kerswell (1999) proposed that a given Kelvin mode can trigger a triad resonance with two other Kelvin modes leading to an instability (this mechanism bears similarity with the mechanism of the elliptic instability). The triggered modes can themselves be unstable leading to a secondary instability and eventually to a tertiary instability, and so on. This cascade of bifurcation may explain the transition to turbulence observed in these flows. When nonlinear effects are important, another aspect of these rotating flows is the generation of a geostrophic motion which slows down the main solid body rotation and modifies its radial profile. Kobine (1995, 1996) has proposed that, due to this geostrophic motion, the main flow can be modified enough to cause a centrifugal instability responsible of the breakdown. Finally the observed breakdown could also be due to a boundary layer instability near the wall of the container. So far, there is no clear experimental evidence to support one of these scenarios.

The picture is different for an ellipsoidal container since there are no corners to prevent the azimuthal circulation. For an inviscid fluid, Poincaré (1910) showed that there exists a class of solution with uniform vorticity whose direction rotates around the precession axis. In a real fluid, the presence of viscous boundary layers selects a unique solution in which the viscous and pressure torques balance the precessional torque (Lorenzani & Tilgner 2001). However, some (conical) inertial waves are still generated by the breakdown of the Ekman layer at a critical latitude (Noir *et al.* 2001). It can lead to an instability consisting of cylindrical waves propagating around the axis of rotation of the fluid (Lorenzani & Tilgner 2001) and generates a strong turbulent flow (Goto *et al.* 2007). It is thus unclear if this flow will be unstable through local destabilisation of the Ekman layers or through a global instability (such as a triadic resonance) for large Reynolds numbers.

In this paper, we address the basic laminar flow in the case of a precessing cylinder full of water. This flow can be decomposed into a sum of Kelvin modes which are resonant if their wavelength is equal to $2H$, $2H/3$, $2H/5$, etc (where H is the cylinder height). By performing Particle Image Velocimetry (PIV) measurements in the precessing frame, we investigate the primary inertial flow in both situations: far from a resonance, where the linear inviscid theory is valid, then close to a resonance, where viscous and non-linear effects determine the amplitude of the resonant Kelvin mode. Gans (1970) first gave a theoretical interpretation of the amplitude saturation close to the resonance by taking into account the viscous effects only. In this paper, the derivation of the amplitude equations is performed by considering both viscous and nonlinear terms. We have distinguished two different regimes of saturation. At low Reynolds numbers, the main mode amplitude is saturated by viscosity (which is consistent with Gans' results (Gans

1970), whereas the nonlinear effects prevail at higher Reynolds numbers (Wood 1965). Such nonlinear couplings of Kelvin modes have been largely studied in the context of the elliptic instability (Waleffe 1989; Eloy *et al.* 2003; Mason & Kerswell 1999).

The paper is organized as follows. Section 2 is dedicated to the general problem formulation. The equations governing the fluid motion are first introduced then the whole experimental setup is presented in details in §2.2. In §3, the linear inviscid theory is presented to express the Kelvin mode amplitudes when the flow is non-resonant. Experimental flow fields are then shown and compared to these theoretical predictions. In §4 the viscous and nonlinear amplitude equations are derived and compared to the PIV velocity fields measured at the resonance. Finally our results are discussed in §5.

2. Presentation of the problem

2.1. *Formulation*

We address the equations governing the flow inside a precessing cylinder full of fluid of density ρ and kinematic viscosity ν. This problem is illustrated in figure 1(a). In the laboratory reference frame (O, $\hat{\mathbf{x}}$, $\hat{\mathbf{y}}$, $\hat{\mathbf{z}}$), we consider a turntable rotating at constant angular frequency $\Omega_2 = \dot{\psi}$ around the axis ($O, \hat{\mathbf{z}}$). In the reference frame of this turntable, a cylinder of radius R_c and height H rotates around its own axis ($O', \hat{\mathbf{k}}$) at the angular frequency $\Omega_1 = \dot{\phi}$. The angle between these two axes of rotation is the nutation angle θ. As shown in figure 1(a), the angles (ψ, θ, ϕ) are the classical Euler coordinates of the cylinder.

In the reference frame of the cylinder (O', $\hat{\mathbf{i}}$, $\hat{\mathbf{j}}$, $\hat{\mathbf{k}}$), the radius vector $\mathbf{R}$ is located by its cylindrical coordinates (R, φ, Z) as shown in figure 1(b). The time-dependent rotation vector of the cylinder in the laboratory frame is

$$\boldsymbol{\Omega} = \Omega_1 \hat{\mathbf{k}} + \Omega_2 \hat{\mathbf{z}}. \tag{2.1}$$

Since the cylinder frame is non galilean, the Navier–Stokes equations satisfied by the velocity field $\mathbf{U}(\mathbf{R}, T)$ and the pressure field $P(\mathbf{R}, T)$ take the following form

$$\frac{\partial \mathbf{U}}{\partial T} + (\mathbf{U} \cdot \boldsymbol{\nabla}) \mathbf{U} + 2 \boldsymbol{\Omega} \times \mathbf{U} + \boldsymbol{\Omega} \times (\boldsymbol{\Omega} \times \mathbf{R}) + \frac{\mathrm{d} \boldsymbol{\Omega}}{\mathrm{d} T} \times \mathbf{R} + \boldsymbol{\Gamma}_{O'} = -\frac{1}{\rho} \boldsymbol{\nabla} P + \nu \Delta \mathbf{U}, \tag{2.2a}$$

and

$$\boldsymbol{\nabla} \cdot \mathbf{U} = 0, \tag{2.2b}$$

with the boundary condition $\mathbf{U} = \mathbf{0}$ on the cylinder walls.

In the Navier–Stokes equation (2.2a), the first two terms are the usual inertial terms, the third and the fourth terms are the Coriolis and centrifugal acceleration respectively, the fifth term is due to the acceleration of the rotation vector and $\boldsymbol{\Gamma}_{O'}$ refers to the acceleration of the centroid O' of the cylinder. Note that this latter term is potential and corresponds to a hydrostatic pressure $\boldsymbol{\Gamma}_{O'} \cdot \mathbf{R}$.

The previous equations are made dimensionless by using R_c and Ω^{-1} as characteristic length and time, where

$$\Omega = \boldsymbol{\Omega} \cdot \hat{\mathbf{k}} = \Omega_1 + \Omega_2 \cos\theta. \tag{2.3}$$

By using lowercase letters for the dimensionless quantities, the Navier–Stokes equations for the dimensionless velocity field $\mathbf{u}(\mathbf{r}, t)$ become

$$\frac{\partial \mathbf{u}}{\partial t} + 2 \hat{\mathbf{k}} \times \mathbf{u} + \boldsymbol{\nabla} p = -2\varepsilon \zeta \omega r \cos(\omega t + \varphi) \hat{\mathbf{k}}$$

$$+ \mathbf{u} \times (\boldsymbol{\nabla} \times \mathbf{u}) - 2\varepsilon \zeta \, \boldsymbol{\delta} \times \mathbf{u} + \frac{1}{Re} \Delta \mathbf{u}, \tag{2.4a}$$

and

$$\boldsymbol{\nabla} \cdot \mathbf{u} = 0, \qquad\qquad (2.4b)$$

with

$$\omega = \frac{\Omega_1}{\Omega}, \ \ \varepsilon = \left| \frac{\Omega_2 \sin\theta}{\Omega} \right|, \ \ \zeta = \operatorname{sgn}\left(\frac{\Omega_2 \sin\theta}{\Omega} \right), \ \ \boldsymbol{\delta} = \cos\omega t\, \hat{\mathbf{i}} - \sin\omega t\, \hat{\mathbf{j}}, \ \ (2.5a\text{–}d)$$

and $Re = \Omega R_c^2/\nu$ the Reynolds number. In this dimensionless form, $h = H/R_c$ is the aspect ratio of the cylinder. The dimensionless pressure field $p(\mathbf{r}, t)$ is constructed to include all the potential terms

$$p = \frac{P}{\rho\, \Omega^2 R_c^2} - \frac{1}{2} r^2 + \varepsilon\, |1 - \omega|\, rz\, \cos(\omega t + \varphi)$$

$$+ \boldsymbol{\gamma}_{O'} \cdot \mathbf{r} - \frac{1}{2}\varepsilon^2 [z^2 + r^2 \sin^2(\omega t + \varphi)] + \frac{1}{2}\mathbf{u}^2, \qquad (2.6)$$

where $\boldsymbol{\gamma}_{O'} = \boldsymbol{\Gamma}_{O'}/R_c\Omega^2$ is the dimensionless acceleration of the cylinder centroid. The boundary condition of the velocity field is

$$\mathbf{u} = \mathbf{0} \quad \text{at the walls } (r = 1 \text{ or } z = \pm h/2). \qquad (2.7)$$

The Navier–Stokes equations (2.4 a, b) with the boundary condition (2.7) govern the flow inside a precessing cylinder. This set of equations has been obtained without any approximation and is thus valid for any value of the experimental parameters. It is clear from these equations that the problem is entirely governed by four dimensionless parameters: the forcing amplitude ε; the forcing frequency ω; the Reynolds number Re; and the cylinder aspect ratio h. However, these equations cannot be solved easily in the general case and we will limit ourselves hereinafter to the case of asymptotically small amplitude ε and large Reynolds number Re. This is the relevant limit if one is interested in the flow forced by the precession before it becomes unstable or at the onset of instability.

For the sake of clarity and brevity, a four-component formulation for the velocity-pressure field $\mathbf{v} = (\mathbf{u}, p)$ expressed in cylindrical coordinates will be used. With this formulation the Navier–Stokes equations (2.4 a, b) take the following form

$$\left(\frac{\partial}{\partial t}\mathcal{I} + \mathcal{M} \right) \mathbf{v} = \varepsilon\zeta\, \mathbf{F}_0 \mathrm{e}^{\mathrm{i}(\omega t + \varphi)} + \mathbf{N}(\mathbf{v}, \mathbf{v}) + \varepsilon\zeta\, \mathcal{D}\, \mathrm{e}^{\mathrm{i}(\omega t + \varphi)}\mathbf{v} + \frac{1}{Re}\mathcal{L}\, \mathbf{v} + \text{c.c.}, \qquad (2.8)$$

where the operators $\mathcal{I}$, $\mathcal{M}$, $\mathcal{D}$, $\mathcal{L}$, the forcing vector $\mathbf{F}_0$ and the bilinear function $\mathbf{N}$ are defined in appendix A. The symbol c.c. stands for the complex conjugate.

We will solve a linearised version of the above equation in §3.1 and the weakly nonlinear and viscous solution corresponding to the saturated resonant flow will be given in §4.1.

2.2. *Experimental setup*

The experimental setup is sketched in figure 2. It corresponds exactly to the configuration depicted in figure 1. A right-circular PMMA cylinder, filled with distilled water, rotates at the angular velocity Ω_1 around its axis and is mounted on a rotating platform. The cylinder axis is tilted relative to the axis of the platform with an angle θ. The platform, that ensures the precessing component of the motion, also rotates at a velocity Ω_2. The platform is mounted on a wide vertical axis in order to limit the vibrations of the structure at high precession velocities.

The angular frequency Ω_1 can be increased up to $60\,\mathrm{rad\,s^{-1}}$ and is measured with an accuracy of 0.1%. The precession frequency Ω_2 is limited to $6\,\mathrm{rad\,s^{-1}}$ and is measured with

an accuracy of 0.2 % when the precession frequency is larger than $0.2 \, \mathrm{rad \, s^{-1}}$. Each axis having its own driving motor, the angular velocities can be varied independently so that the dimensionless frequency ω can be varied over the whole range $[-2, 2]$. We used three different cylinders: a cylinder of aspect ratio $h = H/R_c = 1.989 \pm 0.3\%$ ($H = 9.14 \, \mathrm{cm}$) has been used at first, but its principal resonance was found for a vanishing precessing frequency ($\omega \approx 1$). A second cylinder with aspect ratio $h = 1.8 \pm 0.7\%$ ($H = 8.27 \, \mathrm{cm}$) has been thus designed to study this resonance. Finally, a third cylinder with the same aspect ratio 1.8 but smaller dimensions ($H = 2.7 \, \mathrm{cm}$) has also been used to obtain data at smaller Reynolds numbers (by a factor almost 10). The thickness of the cylinder walls is extremely large (2 cm) in order to avoid shade areas in the light sheet (because of refraction on the cylindrical wall).

The acquisition computer is located on the rotating platform to limit the number of rotating electrical contacts and improve the quality of the data. The power is brought up to the platform by a rotating collector through the vertical axis and is used to supply the cylinder motor, the video camera and the electromagnet of the release device. The rotating collector also conveys back the signal from the video camera to an auxiliary screen, which is used for observation and optical adjustment of the PIV system.

A release device is mounted on the platform and is controlled externally, so that the cylinder can be tilted during the rotation of the platform. It allows the observation of the transient stage during which the observed Kelvin modes grow. The release device is composed of an electromagnet designed to keep the cylinder in a vertical position during the spin-up phase. Once the electromagnet is turned off, a drawback spring pulls the cylinder into its tilted position. The electromagnet is then turned on again to ensure the stability of the nutation angle θ during the experiment. This angle can be varied from 0 to 15 degrees. Due to the spring strength, we consider that the swing of the axis happens in a duration (about half a second) much smaller than the duration of the transient stage (varying from 3 to 50 seconds).

The PIV measurement system is schematically presented in figure 2. The fluid is seeded with small reflecting particles (Optimage Ltd.) of mean diameter 50μm and density $1000 \pm 20 \, \mathrm{kg \, m^{-3}}$. They are illuminated with a light sheet of thickness 2 mm, created either by a Yag pulsed laser for large velocities or by an Argon Ion continuous laser (through an optical fiber) for small velocities. The laser beam goes through a cylindrical lens to provide the laser sheet. None of the lighting system is rotating so the laser sheet is fixed relative to the laboratory frame. As far as the tilt angle θ is not too large (smaller than 5 degrees), the laser sheet, due to its thickness, can be considered normal to the cylinder axis. This might introduce a bias at larger nutation angles and the laser sheet should then be created on the rotating platform with a set of mirrors. The altitude of the laser sheet can be varied along the height of the cylinder and was chosen in a subtle way, depending on the type of experiments that was done. First, to look at the dependence of the amplitude with the frequency ω, we had to take a sheet close to the center of the cylinder (in order to not be at a node of the Kelvin mode): a good compromise was taken as $z = 0.12h$. Then, to study the first (resp. second) resonance of a Kelvin mode, we took $z = h/4$ (resp. $z = h/6$) in order to measure a maximum transverse velocity.

The images of particles are recorded by a PIV camera (Kodak Megaplus ES 1.0, 1008×1018 pixels) mounted on the rotating platform and aligned with the axis of the cylinder. The time interval between two successive images is relatively large (from 5 ms to 1 s) such that the cylinder rotates of approximately 20 degrees between the two images. This creates large displacements of the particles at the periphery of the cylinder (150 pixels), but the two images are rotated around the center of the cylinder in order to remove the solid body rotation of the particles. The PIV thus gives directly the velocity field in the

cylinder reference frame. This procedure allows to measure very small velocities down to 1% of the velocity of the cylinder wall. Such measurements would not have been possible without the image rotation. The pairs of images are then treated by a cross-correlation algorithm detailed in Meunier & Leweke (2003) which gives velocity fields with 60×60 vectors.

To perform the acquisition of a PIV field, we proceed as follows. First the cylinder is kept vertical and rotates at Ω_1. The platform rotates at Ω_2 so that the angular velocity of the cylinder relative to the laboratory frame is $(\Omega_1 + \Omega_2)\,\hat{\mathbf{z}}$. Once the spin-up stage is completed, the cylinder is released to its tilted position. This allows to study the transient and the spin-up phase independently.

Some preliminary visualisations were also performed with Kalliroscope particles, in order to check that the resonances were in good agreement with the linear inviscid theory, and to validate our set-up by comparison of these visualisations with those from the literature (Manasseh 1992; Kobine 1995). However, no quantitative new results were obtained and we will not present any of these visualisations in this paper.

3. Flow inside a non-resonant cylinder

3.1. *Linear inviscid theory*

We assume an asymptotically small forcing amplitude ε and asymptotically large Reynolds number Re. In this limit, the velocity-pressure field $\mathbf{v}$ is $O(\varepsilon)$ and the Navier–Stokes equation (2.8) becomes at first order in ε

$$\left(\frac{\partial}{\partial t}\mathcal{I} + \mathcal{M}\right)\mathbf{v} = \varepsilon\zeta\,\mathbf{F}_0\mathrm{e}^{\mathrm{i}(\omega t+\varphi)} + \text{c.c.} \qquad (3.1)$$

For an inviscid fluid, the no-slip boundary condition (2.7) becomes a condition of no outward flow

$$\mathbf{u}\cdot\mathbf{n} = 0 \quad \text{at the walls } (r = 1 \text{ or } z = \pm h/2), \qquad (3.2)$$

where $\mathbf{n}$ is an unitary vector normal to the wall.

Equations (3.1) and (3.2) form a linear system for the vector $\mathbf{v} = (\mathbf{u},\,p)$, with a forcing term. It admits a particular solution of the form

$$\mathbf{v}_{\text{part.}} = (0,\,0,\,\varepsilon\,\zeta\,\mathrm{i}\,r\,\mathrm{e}^{\mathrm{i}(\omega t+\varphi)},\,0) + \text{c.c.} \qquad (3.3)$$

Unfortunately, this solution does not satisfy the boundary condition (3.2) in $z = \pm h/2$. Thus, one must complete this particular solution with a solution of the homogeneous equation (without forcing), so that the boundary condition at the upper and lower walls is satisfied. Due to the time and azimuthal dependence of the forcing, the homogeneous solution is to be searched as a sum of Kelvin modes of azimuthal wavenumber $m = 1$ and angular frequency ω (see Greenspan 1968). Using (3.2) and (3.3) and such a form of the homogeneous solution, one finds

$$\mathbf{v} = \mathbf{v}_{\text{part.}} + \varepsilon\,\zeta\,\sum_{i=1}^{\infty} a_i\mathbf{v}_i(r,\,z)\mathrm{e}^{\mathrm{i}(\omega t+\varphi)} + \text{c.c.}, \qquad (3.4)$$

where $\mathbf{v}_i(r,\,z)\mathrm{e}^{\mathrm{i}(\omega t+\varphi)}$ is a Kelvin mode of axial wavenumber k_i, azimuthal wavenumber

$m = 1$ and frequency ω

$$\mathbf{v}_i(r,\,z) = \begin{pmatrix} u_i(r)\,\sin(k_i z) \\ v_i(r)\,\sin(k_i z) \\ w_i(r)\,\cos(k_i z) \\ p_i(r)\,\sin(k_i z) \end{pmatrix} \quad \text{with} \quad \begin{cases} u_i(r) = \mathrm{i}\dfrac{\omega r \delta_i\,J_1'(\delta_i r) + 2 J_1(\delta_i r)}{r(\omega^2 - 4)} \\[2ex] v_i(r) = \dfrac{2 r \delta_i\,J_1'(\delta_i r) + \omega J_1(\delta_i r)}{r(4 - \omega^2)} \\[2ex] w_i(r) = \dfrac{\mathrm{i}\,k_i}{\omega} J_1(\delta_i r) \\[2ex] p_i(r) = J_1(\delta_i r) \end{cases} \quad , \quad (3.5)$$

with $J_\nu(x)$ the Bessel function of the first kind and $J_\nu'(x)$ its x-derivative. The amplitude a_i of each Kelvin mode is

$$a_i = \frac{2\,\omega^2}{(\omega - 2)(k_i^2 + 1)\,k_i\,J_1(\delta_i)\cos(k_i\,h/2)}, \qquad (3.6)$$

the axial wavenumber k_i is the positive root of the constitutive relation

$$\delta_i^2 = \frac{4 - \omega^2}{\omega^2} k_i^2, \qquad (3.7)$$

and the radial wavenumber δ_i is solution of Kelvin's dispersion relation

$$\omega\,\delta_i\,J_1'(\delta_i) + 2 J_1(\delta_i) = 0. \qquad (3.8)$$

As long as $-2 < \omega < 2$, the dispersion relation admits an infinite, countable number of roots δ_i which are numbered in ascending order. A Kelvin mode can be associated to each root δ_i. The radial velocity $u_i(r)$ of the first Kelvin mode (corresponding to δ_1) is formed of one lobe and has no zero for $0 < r < 1$, the second Kelvin mode contains two lobes and one zero, the third contains three lobes and two zeros, and so on. The velocity field of the first Kelvin mode is shown in Fig. 3(a): it contains two counter-rotating vortices, due to the presence of a single lobe of radial velocity and an azimuthal wavenumber $m = 1$. In the general case, the i-th Kelvin mode contains $2i$ vortices, and these Kelvin modes form a complete set. Their dispersion relation (3.7-3.8) is plotted on Fig. 4. The precession excites only the Kelvin modes with a given frequency ω corresponding to increasing wavenumbers k_i (as shown on Fig. 4 for $\omega = \omega_{3,4}$). When the wavenumber k_i of a Kelvin mode is equal to π/h, $3\pi/h$, $5\pi/h$... the mode 'fits' inside the height of the cylinder and becomes resonant. When ω is increased, each branch of the dispersion relation leads to an infinite number of resonances, with the wavenumber k_i of the Kelvin mode being equal to $\pi(2n-1)/h$ (n being an integer). Strictly speaking, each resonance labeled with (i, n) corresponds to a different Kelvin mode. In the following, all modes corresponding to the same branch of the dispersion relation (same index i) will be gathered in a family of modes which will be called the i-th Kelvin mode (for the sake of simplicity).

   Equation (3.6) gives the amplitudes of the Kelvin modes forced by the precession. This equation is valid as long as the cylinder aspect ratio is not resonant, i.e. $\cos(k_i h/2) \neq 0$. In other words, the present linear analysis predicts a divergent amplitude of the i-th Kelvin mode if the forcing frequency ω is equal to one of the natural frequencies $\omega_{i,n}$ of the cylinder. Here, $\omega_{i,n}$ refers to the frequency obtained through (3.7) and (3.8) by taking $k_i = \pi(2n-1)/h$, with n an integer. One can show (Kudlick 1966) that the set of natural frequencies $\omega_{i,n}$ is dense in the interval $-2 < \omega < 2$. This means that there is always a Kelvin mode arbitrary close to a resonance for any chosen forcing frequency ω. This emphasises the need of a theoretical prediction of the Kelvin mode amplitude at the resonance as it will be done in §4.1.

3.2. *Kelvin modes: PIV measurements*

We performed PIV measurements of the (u, v) transverse velocity field in the range $0.2 < \omega < 1.9$ and at Reynolds numbers between 2×10^3 and 2×10^5. The issue was, from the averaged velocity field in the permanent regime, to achieve the extraction of the linear amplitudes a_i of the main modes as defined by (3.6).

In figure 3(a) is shown the horizontal-velocity field at a frequency $\omega = 0.9$ close to the first resonance $\omega_{1,1} = 0.996$ of the mode $i = 1$, for $Re = 5500$ and $\theta = 1°$, the laser sheet being at an altitude $z = 0.29$. As previously mentionned, the flow in the reference frame of the cylinder mainly consists of two counter rotating vortices corresponding to the first Kelvin mode described by the above inviscid theory. However, it can be noted that the mode is not exactly aligned with the x_ψ-axis. This tilt angle is due to the viscous and nonlinear effects appearing at the resonance and will be analysed in detail in the next section. Figure 3(b) shows the radial velocity profile along the x_ψ-axis of this velocity field, as round symbols. The normalised value of the velocity decreases monotonically between $r = 0$ and $r = 1$, and is very close to the curve found theoretically (solid line) for the first Kelvin mode at this value of ω. Figure 3(b) also shows the radial velocity profile obtained for $\omega = 0.45$, i.e. close to the resonance of the second mode. It exhibits a positive lobe for $r < 0.5$, a negative lobe for $r > 0.5$ and a zero for $r \simeq 0.5$. This is characteristic of the second Kelvin mode, whose theoretical radial velocity is plotted as a dashed line. The third Kelvin mode (plotted as a dotted line) has three lobes of opposite radial velocity, but in this case the experimental data are very noisy and have not been plotted.

The presence of these Kelvin modes is better visualised by plotting the mean vorticity fields as done in Fig. 5, since the small scatter in the velocity field (such as a translation or a rotation) is hidden by the differentiation of **u** and the modification of the colorbar. The Kelvin modes are thus clearly distinguished by plotting the vorticity fields at various ω: even the fifth Kelvin mode is discernible at its first resonance $\omega_{5,1} = 0.2$. However, the spatial structure is arranged as a double spiral for the highest modes, whereas the theory predicts a series of lobes since the vorticity is expected to vanish for $\varphi = \pi/2 - \omega t$. In fact, such a spiral structure has already been observed theoretically for the Kelvin modes of a Gaussian vortex by Fabre *et al.* (2006). We thus think that this discrepancy might be due to a slight differential rotation in the geostrophic motion, coming from nonlinear and viscous effects.

For each experiment outside of the resonance, we have decomposed each velocity field into a sum of Kelvin modes. For this purpose, we use the fact that the Kelvin modes are orthogonal, such that the amplitude a_i of each Kelvin mode is simply given by the normalised scalar product $\langle \mathbf{u}_{\mathrm{exp}} | \mathbf{u}_i \rangle / \langle \mathbf{u}_i | \mathbf{u}_i \rangle$ (see appendix B for exact definition), where $\mathbf{u}_{\mathrm{exp}}$ (resp. $\mathbf{u}_i$) are the two transverse components of the measured (resp. theoretical) velocity field and the scalar product is defined as the average over the whole section. In fact, the method has to be slightly improved since this average can only be calculated for $r \leq 0.9$ instead of $r \leq 1$ (due to spurious vectors at the cylinder wall) and because the mode can have a tilt angle α_i with respect to the x_ψ axis. This method, which is detailed in appendix B, allows the precise determination of the amplitude and tilt angle of the first two Kelvin modes for each instantaneous velocity field.

In the permanent regime, the amplitude of the Kelvin modes is stationary and depends only on the frequency ω. It is plotted in Fig. 6 for the first two Kelvin modes and for two different Reynolds numbers. Despite a large scatter, experimental results are clearly independent of the Reynolds number outside of the resonances and very well predicted by the linear inviscid theory. As far as we know, this is the first exact measurement of

the mode amplitudes forced by precession. The amplitudes measured at the resonances, for the first two modes are large and cannot be predicted by the linear inviscid theory. A nonlinear and viscous theory is necessary to predict the finite value of the amplitude in this case; this is the scope of §4.

3.3. *Transient stage*

The experimental results can also give indications on the transient stage, since the amplitude a_i of each mode can be extracted for each instantaneous velocity field. Fig. 7(a) shows the temporal evolution of the amplitude of the first Kelvin mode just after the onset of the precession forcing, far from its resonance. The amplitude oscillates very rapidly and converges toward its permanent value a_1^0 which is plotted in Fig. 6. This curve can be fitted by a decaying exponential $a_1(t) = a_1^0[1 - \cos(\omega_t t)e^{-t/t_s}]$ where ω_t corresponds to the frequency of the oscillation and t_s is the settling time. Since ω_t corresponds to the frequency in the rotating table reference frame, we have to subtract the dimensionalised angular velocity of the cylinder ω to obtain the frequency of the oscillation in the cylinder reference frame. By doing this, we find a non-dimensional frequency $\omega_t - \omega$ close to -1.8, and this was observed for any ω outside of a resonance. This value is close to the frequency of the second resonance of the first Kelvin mode $\omega_{1,2} = 1.774$. This can be understood by the fact that at $t = 0^+$, the velocity field which is equal to 0 in the bulk of the cylinder is the sum of the permanent solution (given by the inviscid theory) and a sum of free and decaying Kelvin modes with frequencies $-2 < \omega_{i,n} < 2$, n varying from 1 to infinity. Another methof to evaluate experimentally the initial amplitude of each free Kelvin mode is to plot the Fourier transform of the amplitude as a function of the dimensionalised frequency $\omega_t - \omega$, as shown on Fig. 7(b). A small peak is discernible around -1 (for both values of ω), which corresponds to the free Kelvin mode $\omega_{1,1} = 0.996$ and which is indicated by a thin solid line on the figure. A large peak is located near -1.8, which is close to all the other free Kelvin modes (with $i = 1$), whose frequencies $(\omega_{1,n})_{n\geq 2}$ lie between 1.774 and 2. It is thus not clear whether this large peak is due to a large amplitude of the second free Kelvin mode $\omega_{1,2}$ or to the constructive interference of all these modes $(\omega_{1,n})_{n\geq 2}$.

4. Flow inside a resonant cylinder

4.1. *Nonlinear and viscous theory*

As seen in §3.1, when the forcing frequency ω is equal to a natural frequency of the cylinder $\omega_{i,n}$, the linear inviscid theory predicts a divergent amplitude of the i-th Kelvin mode. To predict correctly the mode amplitude in this case, one has to take into account the viscous effects or the nonlinear effects or both. As shown by Gans (1970), if A_i is the mode amplitude, the secondary flow in the core of the cylinder due to the viscous boundary layers is $O(A_i Re^{-1/2})$. If the nonlinear effects are negligible, the correct scaling is obtained when this secondary flow is of the order of the forcing amplitude ε. This gives a mode amplitude $A_i = O(\varepsilon Re^{1/2})$ which is $Re^{1/2}$ larger than the flow in the non-resonant case. On the other hand, if the viscous effects are negligible, the secondary flow is due to the nonlinear interaction of the Kelvin mode with itself. In this case, the secondary flow of same Fourier components is obtained at third order and is $O(|A_i|^2 A_i)$. This gives a mode amplitude $A_i = O(\varepsilon^{1/3})$.

The distinguished scaling is obtained when the viscous and nonlinear effects are of same order, that is $\varepsilon^{2/3} = O(Re^{-1/2})$. This leads to the definition of a viscous parameter

η of order 1 and a slow time scale τ as follows

$$\eta = Re^{-1/2}\varepsilon^{-2/3}, \quad \tau = \varepsilon^{2/3}t. \qquad (4.1a,b)$$

We now assume that the forcing frequency ω is close to a resonant frequency $\omega_{i,n}$ for the i-th Kelvin mode. The four-component velocity-pressure field corresponding to this Kelvin mode is expanded in powers of $\varepsilon^{1/3}$ as follows

$$\mathbf{V}_i = \varepsilon^{1/3}\,\mathbf{V}_1 + \varepsilon^{2/3}\,\mathbf{V}_2 + \varepsilon\,\mathbf{V}_3 + \varepsilon^{4/3}\,\mathbf{V}_4 + \cdots. \qquad (4.2)$$

The real velocity field is obtained by adding the complex conjugate in the above equation (the same is implicitly assumed in all the following equations). The nonlinear and viscous amplitude equations are obtained by injecting the above expansion (4.2) into the Navier–Stokes equation (2.8) and examining its different orders. The procedure is similar to the one used by Gans (1970) except that here the nonlinear effects are included and the forcing frequency ω is arbitrary, whereas Gans (1970) considered only the special case $\omega = 1$ which corresponds to a nutation angle $\theta = \pi/2$. The present analysis bears strong similarities with the weakly nonlinear analysis of parametric instabilities in rotating flows such as the elliptic instability (Waleffe 1989; Sipp 2000; Eloy *et al.* 2003) or the instability of a rotating gas periodically compressed (Racz & Scott 2007). Because this calculation is quite lengthy, most of its technical details have been postponed in appendices C, D and E.

4.1.1. *Order $\varepsilon^{1/3}$*

At order $\varepsilon^{1/3}$, the resonant flow satisfying the linear homogeneous equation

$$\left(\frac{\partial}{\partial t}\mathcal{I} + \mathcal{M}\right)\mathbf{V}_1 = \mathbf{0}, \qquad (4.3)$$

is

$$\mathbf{V}_1 = A(\tau)\,\mathbf{v}_i\,\mathrm{e}^{\mathrm{i}(\omega t + \varphi)}, \qquad (4.4)$$

where $\mathbf{v}_i$ is the i-th Kelvin mode given by (3.5), as it has been shown in §3.1. The amplitude A of the Kelvin mode $\mathbf{v}_i$ is assumed to vary on the slow time scale τ and the other Kelvin modes (with $j \neq i$) are assumed to be non resonant so their amplitudes are given by (3.6).

The Kelvin mode $\mathbf{v}_i$ satisfies an inviscid boundary conditions. In a viscous boundary layer of thickness $O(Re^{-1/2})$, the complete flow is obtained by adding the viscous flow $\widetilde{\mathbf{V}}_1$ such that $\mathbf{V}_1 + \widetilde{\mathbf{V}}_1$ satisfies the viscous boundary condition (2.7). This viscous flow takes the form

$$\widetilde{\mathbf{V}}_1 = A\,\widetilde{\mathbf{v}}_i\,\mathrm{e}^{\mathrm{i}(\omega t + \varphi)}, \qquad (4.5)$$

where $\widetilde{\mathbf{v}}_i$ is the viscous counterpart of the Kelvin mode $\mathbf{v}_i$ located in a viscous boundary layer of thickness $O(Re^{-1/2})$ near the walls (its complete expression is given in appendix D). At this order the viscous flow $\widetilde{\mathbf{v}}_i$ is parallel to the walls (it has to compensate $\mathbf{V}_1$ which is also parallel to the wall because of the inviscid boundary condition). However, this viscous flow gives rise to an Ekman pumping at order ε with a component perpendicular to the walls $\widetilde{\mathbf{V}}_3^{\perp} = O(\eta\widetilde{\mathbf{V}}_1)$. This gives a boundary condition for the inviscid flow at order ε:

$$\mathbf{V}_3 \cdot \mathbf{n} = -\widetilde{\mathbf{V}}_3^{\perp} = -\eta A\,\widetilde{\mathbf{v}}_3 \cdot \mathbf{n}\,\mathrm{e}^{\mathrm{i}(\omega t + \varphi)} \quad \text{on the walls}, \qquad (4.6)$$

where $\mathbf{n}$ is the unitary vector normal to the wall and $\widetilde{\mathbf{v}}_3 \cdot \mathbf{n}$ is a function of order 1 given in appendix D.

4.1.2. *Order $\varepsilon^{2/3}$*

As shown by Greenspan (1969), the nonlinear interaction of a Kelvin mode with itself gives rise to two velocity components. For a Kelvin mode of wavenumbers-frequency (k, m, ω) (where m is the azimuthal wavenumber, in our case $m = 1$), these two components are of the form $(2k, 0, 0)$ and $(0, 2m, 2\omega)$. In other words, the geostrophic mode $(0, 0, 0)$ and the mode $(2k, 2m, 2\omega)$ are not forced by nonlinear interactions.

At order $\varepsilon^{2/3}$ the Navier–Stokes equation (2.8) becomes

$$\left(\frac{\partial}{\partial t} \mathcal{I} + \mathcal{M} \right) \mathbf{V}_2 = \mathbf{N}(\mathbf{V}_1, \mathbf{V}_1). \tag{4.7}$$

The solution of this equation is

$$\mathbf{V}_2 = |A|^2 \, \mathbf{v}_{2k} + A^2 \, \mathbf{v}_{2\omega} e^{i(2\omega t + 2\varphi)} + \sum_{j=1}^{\infty} A_0^j(\tau) \mathbf{v}_0^j + \text{o.t.}, \tag{4.8}$$

where o.t. stands for 'other terms' of different Fourier components. The first two terms of (4.8) correspond to the particular solution of (4.7) (see Waleffe 1989). In agreement with Greenspan (1969), they are of the form $(2k, 0, 0)$ and $(0, 2, 2\omega)$ (these velocity fields are given explicitly in appendix C).

The third term of (4.8) is the solution of (4.7) without forcing, where we have only retained the axisymmetric geostrophic modes of Fourier components $(k, m, \omega) = (0, 0, 0)$. It is easy to show that this flow is a stationary azimuthal velocity field whose components can be written as $\mathbf{v}_0^j = (0, v_0^j(r), 0, p_0^j(r))$ in cylindrical coordinates. At this point, the geostrophic flow is arbitrary and we choose to decompose it on the basis of the Bessel functions of the first kind such that

$$v_0^j(r) = -J_1(d_j r) \quad \text{with} \quad J_1(d_j) = 0, \tag{4.9}$$

with the roots d_j sorted in ascending order such that $d_j = j\pi + O(1)$. We chose to put a minus sign in the above expression such that a positive amplitude A_0^j corresponds to a slow down of the basic solid body rotation. As we will see below, this geostrophic flow is forced at order $\varepsilon^{4/3}$ by the nonlinear interactions in the end wall boundary layers. Its saturation is due to viscous effects in the boundary layers and this geostrophic mode therefore appears at order $A_0 = O(\varepsilon^{4/3} Re^{1/2}) = O(\varepsilon^{2/3})$.

The velocity field $\mathbf{V}_2$ satisfies inviscid boundary conditions. As we did at order $\varepsilon^{1/3}$, one has to add a viscous velocity field $\widetilde{\mathbf{V}}_2$ in a boundary layer of thickness $O(Re^{-1/2})$ in order to satisfy the viscous boundary condition at the walls. This viscous flow is decomposed into several components. First, the velocity fields $\mathbf{v}_{2k}$ and $\mathbf{v}_{2\omega}$ contribute to this viscous velocity field. Then the geostrophic flow corresponds to viscous corrections $\widetilde{\mathbf{v}}_0^j$ in the end wall boundary layers. And finally, the nonlinear interactions of $\mathbf{V}$ with $\widetilde{\mathbf{V}}$ and $\widetilde{\mathbf{V}}$ with itself act as a source term at order $\varepsilon^{2/3}$ and give rise to a nonlinear part of the viscous flow $\widetilde{\mathbf{V}}_2^{\text{NL}}$. If we are only interested in the axisymmetric and stationnary part of this viscous flow, it can be written as

$$\widetilde{\mathbf{V}}_2 = |A|^2 \, \widetilde{\mathbf{v}}_{2k} + |A|^2 \widetilde{\mathbf{v}}_2^{\text{NL}} + \sum_{j=1}^{\infty} A_0^j(\tau) \widetilde{\mathbf{v}}_0^j + \text{o.t.}, \tag{4.10}$$

where the details of these velocity fields are given in appendices D and E. This viscous flow $\widetilde{\mathbf{V}}_2$ is parallel to the walls at this order but it gives rise to an Ekman pumping at the end walls at the order $\varepsilon^{4/3}$ of the form $\widetilde{\mathbf{V}}_4^{\perp} = O(\eta \widetilde{\mathbf{V}}_2)$. This pumping gives a boundary

condition for the inviscid flow of the form

$$\mathbf{V}_4 \cdot \mathbf{n} = -\widetilde{\mathbf{V}}_4^\perp = -\eta |A|^2 \widetilde{\mathbf{v}}_4^{\mathrm{NL}} \cdot \mathbf{n} - \eta \sum_{j=1}^\infty A_0^j(\tau) \widetilde{\mathbf{v}}_4^j \cdot \mathbf{n} + \text{o.t.}, \quad \text{on the walls}, \qquad (4.11)$$

where the details of these fields are given in appendices D and E and where we have omitted the term due to $\widetilde{\mathbf{v}}_{2k}$ because it does not contribute to the forcing of the geostrophic mode at order $\varepsilon^{4/3}$ as it will be shown below.

4.1.3. *Order ε*

At order ε, the Navier–Stokes equation becomes

$$\mathcal{I} \frac{\partial \mathbf{V}_1}{\partial \tau} + \left(\frac{\partial}{\partial t} \mathcal{I} + \mathcal{M} \right) \mathbf{V}_3 = \zeta \, \mathbf{F}_0 \mathrm{e}^{\mathrm{i}(\omega t + \varphi)} + \mathbf{N}(\mathbf{V}_1, \mathbf{V}_2) + \mathbf{N}(\mathbf{V}_2, \mathbf{V}_1) + \frac{\eta \mathcal{L} \mathbf{V}_1}{Re^{1/2}}. \quad (4.12)$$

The last term of this equation should not appear at this order but at order $\varepsilon^{5/3}$. However, we have decided to take it into account in the analysis because its importance in evaluating the viscous decay has been shown in several papers (Kerswell & Barenghi 1995; Eloy *et al.* 2003; Racz & Scott 2007). The integration of equation (4.12) is not needed. We introduce the scalar product

$$\mathbf{X} \odot \mathbf{Y} = \int_V (\overline{X}_r Y_r + \overline{X}_\varphi Y_\varphi + \overline{X}_z Y_z + \overline{X}_p Y_p) \mathrm{d}^3 V, \qquad (4.13)$$

where the overbar stands for complex conjugation and V is the volume of the cylinder. A solvability condition for $\mathbf{V}_3$ is obtained by forming the scalar product of $\mathbf{v}_i \, \mathrm{e}^{\mathrm{i}(\omega t + \varphi)}$ with the equation (4.12) and dividing by $\mathbf{v}_i \odot \mathcal{I} \, \mathbf{v}_i$. It yields the following amplitude equation for A

$$\frac{\partial A}{\partial \tau} = \mathrm{i} f - \eta \left(\mu + \frac{\nu}{Re^{1/2}} \right) A + \mathrm{i} \left(\sigma |A|^2 - \sum_{j=1}^\infty \xi_j A_0^j \right) A, \qquad (4.14)$$

where the calculation of the different coefficients is detailed in appendices D and C. Some useful numerical values are given in Tables 1–3. In the above equation the term f comes from the forcing $\mathbf{F}_0$, the term ν is linked to the volume viscous damping. The term σ originates from the nonlinear interaction of $\mathbf{V}_1$ with $\mathbf{v}_{2k}$ and $\mathbf{v}_{2\omega}$. The terms ξ_j come from the nonlinear interaction of $\mathbf{V}_1$ with the geostrophic modes $\mathbf{v}_0^j$. The surface viscous damping term μ comes from the following relation

$$\mathbf{v}_i \, \mathrm{e}^{\mathrm{i}(\omega t + \varphi)} \odot \left(\frac{\partial}{\partial t} \mathcal{I} + \mathcal{M} \right) \mathbf{V}_3 = \int_S \overline{p_i} \, \mathrm{e}^{-\mathrm{i}(\omega t + \varphi)} \mathbf{V}_3 \cdot \mathbf{n} \, \mathrm{d}^2 S = \eta \mu A \left(\mathbf{v}_i \odot \mathcal{I} \, \mathbf{v}_i \right), \quad (4.15)$$

where S is the surface of the cylinder. This relation is obtained by integrating by parts the scalar product and using the fact that $\mathbf{v}_i \, \mathrm{e}^{\mathrm{i}(\omega t + \varphi)}$ is in the kernel of the operator $(\partial \mathcal{I}/\partial t + \mathcal{M})$ by construction. Since $\mathbf{V}_3 \cdot \mathbf{n}$ is known from the relation (4.6) and is proportional to ηA, the above relation leads to the evaluation of μ in (4.14). This term is a complex number whereas all the other coefficients of (4.14) are real. This means that the viscous boundary layers have two effects: the damping of the flow (the real part of μ is positive) and a detuning of the resonance (due to the non-zero imaginary part of μ).

i,n	$\omega_{i,n}$	δ_i	f	μ	σ	ξ	ν
1,1	1.088	2.691	-0.467	$1.799 - 0.268i$	-0.058	1.524	10.3
1,2	1.812	2.447	0.0328	$0.822 - 0.456i$	11.37	170.2	33.4
1,3	1.927	2.420	-0.00522	$0.486 - 0.342i$	76.03	1897	82.0
2,1	0.566	5.912	-0.0771	$1.707 + 0.041i$	-9.13	2.736	38.0
2,2	1.366	5.602	-0.0187	$1.434 - 0.382i$	15.35	75.51	58.8

TABLE 1. Values of the nonlinear and viscous parameters for an aspect ratio $h = 1.8$.

4.1.4. *Order $\varepsilon^{4/3}$*

At order $\varepsilon^{4/3}$, if we retain only the geostrophic terms, the Navier–Sokes equation becomes

$$\sum_{j=1}^{\infty} \frac{\partial A_0^j}{\partial \tau} \mathcal{I} \, \mathbf{v}_0^j + \mathcal{M} \mathbf{V}_4 = \sum_{j=1}^{\infty} \frac{\eta \, A_0^j}{Re^{1/2}} \mathcal{L} \, \mathbf{v}_0^j + \text{o.t.}, \qquad (4.16)$$

where the volume viscous term on the right hand side has been included for the same reason as in (4.12). The terms $\mathbf{N}(\mathbf{V}_2, \mathbf{V}_2)$ and $\mathbf{N}(\mathbf{V}_1, \mathbf{V}_3)$ do not appear in the above equation because they do not lead to geostrophic forcing.

The amplitude equation for the geostrophic mode can be found by forming the scalar product [as defined by (4.13)] of $\mathbf{v}_0^j$ with (4.16) and dividing by $\mathbf{v}_0^j \odot \mathcal{I} \, \mathbf{v}_0^j$. It yields the amplitude equations for the geostrophic modes

$$\frac{\partial A_0^j}{\partial \tau} = \eta \chi_j |A|^2 - \eta \left(\frac{2}{h} + \frac{d_j^2}{Re^{1/2}} \right) A_0^j. \qquad (4.17)$$

The last term comes from volume viscous effects by using the following equality

$$\mathbf{v}_0^j \odot \mathcal{L} \, \mathbf{v}_0^j = -d_j^2 \, \mathbf{v}_0^j \odot \mathcal{I} \, \mathbf{v}_0^j. \qquad (4.18)$$

The forcing term χ_j and the surface viscous damping $2/h$ originate from the relation

$$\mathbf{v}_0^j \odot \mathcal{M} \mathbf{V}_4 = \int_S p_0^j \, \mathbf{V}_4 \cdot \mathbf{n} \, \mathrm{d}^2 S = \eta \left(-\chi_j |A|^2 + \frac{2}{h} A_0^j \right) \left(\mathbf{v}_0^j \odot \mathcal{I} \, \mathbf{v}_0^j \right), \qquad (4.19)$$

where we have integrated by parts the scalar product and used the fact that $\mathbf{v}_0^j$ is in the kernel of $\mathcal{M}$. The outward velocity $\mathbf{V}_4 \cdot \mathbf{n}$ is known from the relation (4.11); it allows to calculate the coefficients χ_j and $2/h$ as it is detailed in appendices D and E. Here, the term due to $\widetilde{\mathbf{v}}_{2k}$ in $\mathbf{V}_4 \cdot \mathbf{n}$ has no influence since we only retained the geostrophic part of the flow (independent of z) in (4.16). Physically, the forcing of the geostrophic mode appears through the coefficient χ_j and is due to the nonlinear interaction of the flow with itself in the end wall boundary layers. Therefore, to have a geostrophic flow, both nonlinear and viscous effects are needed near the end walls.

4.2. *Discussion*

In this section, we will discuss the results of the nonlinear viscous theory presented in §4.1 and compare it with experimental measurements.

4.2.1. *Amplitude equations*

The amplitude equations (4.14) and (4.17) give the time dependence of the Kelvin mode amplitude A and the amplitudes A_0^j of the geostrophic modes. A further simplification can be obtained by assuming that the Reynolds number is large when the nonlinear

i,n	$\omega_{i,n}$	δ_i	f	μ	σ	ξ	ν
1,1	0.996	2.737	0.469	$1.728 - 0.128i$	-0.232	0.910	9.96
1,2	1.774	2.456	0.0418	$0.841 - 0.404i$	7.799	94.28	28.2
1,3	1.911	2.424	-0.00696	$0.497 - 0.322i$	50.93	1032	67.6
2,1	0.510	5.960	-0.0737	$1.579 + 0.112i$	-10.69	1.921	38.0
2,2	1.285	5.618	-0.0209	$1.398 - 0.261i$	9.962	45.70	53.8

TABLE 2. Values of the nonlinear and viscous parameters for an aspect ratio $h = 2$.

i,n	h	ξ_1	ξ_2	ξ_3	ξ_4	ξ_5	χ_1	χ_2	χ_3	χ_4	χ_5
1,1	1.8	0.277	0.144	-0.052	0.031	-0.021	4.743	1.308	-0.314	0.139	-0.077
1,2	1.8	0.701	0.062	-0.017	0.009	-0.006	240.2	27.56	-7.231	3.253	-1.811
1,3	1.8	0.767	0.049	-0.011	0.005	-0.003	2458	244.3	-64.13	28.82	-16.03
2,1	2	-0.516	-0.132	0.316	0.127	-0.044	2.331	-1.044	7.969	3.388	-0.907

TABLE 3. Values of the first parameters ξ_i and χ_i for different resonances i, n and different aspect ratios h.

effects come into play. In this case, the volume viscous term $d_j^2 Re^{-1/2}$ can be neglected in front of the surface viscous term $2/h$ for the geostrophic modes. With this assumption, all geostrophic modes have the same natural decay time and one can define a single geostrophic amplitude $A_0 = A_0^j/\chi_j$ such that all amplitude equations for the geostrophic modes become identical. By defining a global parameter $\xi = \sum_{j=1}^{\infty} \chi_j \xi_j$, the final system can be reduced to two amplitude equations:

$$\frac{\partial A}{\partial \tau} = \mathrm{i} f \left(1 - \frac{A}{\varepsilon^{2/3} a_i} \right) - \eta \left(\mu + \frac{\nu}{Re^{1/2}} \right) A + \mathrm{i} \left(\sigma |A|^2 - \xi A_0 \right) A, \qquad (4.20a)$$

$$\frac{\partial A_0}{\partial \tau} = \eta \left(|A|^2 - \frac{2}{h} A_0 \right). \qquad (4.20b)$$

In these equations, we have assumed that the frequency ω is not exactly equal to the resonant frequency $\omega_{i,n}$, which introduces an additional axial velocity in the solvability condition at order ε, leading to the extra term $\mathrm{i} f A/(\varepsilon^{2/3} a_i)$, where a_i is the amplitude of the Kelvin mode given by (3.6). This term vanishes at the resonance since a_i diverges in this case. On the other hand, if the forcing frequency is far enough, the resonant frequency such that $a_i \ll \varepsilon^{2/3}$, we recover the inviscid solution $A = \varepsilon^{2/3} a_i$ of § 3.1.

The linear forcing parameter f and the nonlinear parameter σ (corresponding to the interaction of the Kelvin mode with itself) are given analytically in Appendix C. The surface and volume viscous parameters μ and ν are given in Appendix D. The term ξ is due to the nonlinear interaction of the Kelvin mode with the geostrophic modes and cannot be given analytically in a simple form. We thus show the variation of this parameter as a function of the aspect ratio h in Fig. 8 for five different resonances. It drastically decreases of ten decades when h increases from 0.1 to 10. This is due to the fact that the nonlinear forcing of the geostrophic mode is generated in the top and bottom boundary layers only, and is thus more efficient for small aspect ratios h.

The amplitude equations (4.20 a, b) describe the transient stage and the saturation of the mode amplitude A. They have been obtained for the distinguished scaling $\varepsilon^{2/3} = O(Re^{-1/2})$ which corresponds to $\eta = O(1)$. However, one can easily obtain simplified equations when viscous effects are dominant by taking the limit $\eta \gg 1$. In this case,

the amplitude equation for the geostrophic mode (4.20 b) is not needed anymore and the amplitude equation (4.20 a) simplifies into a linear equation for A with a forcing term. Its solution is an exponential convergence toward a fixed point with a characteristic time scale which is the natural viscous decay time of the Kelvin mode. The fixed point corresponds to $A = O(\eta^{-1})$ which gives $\mathbf{V}_i = O(\varepsilon Re^{1/2})$ in agreement with the results of Gans (1970). In this case, it is easy to show that the mode amplitude is maximum when the detuning of the forcing frequency compensates exactly the viscous detuning, i.e. $f/(\varepsilon^{2/3} a_i) = -\eta \operatorname{Im}(\mu)$. When this is true, A is a pure imaginary number, which means that the mode is oriented with an angle of $\pi/2$ compared to the non-resonant case of §3.1.

When nonlinear effects are not negligible, the dynamics of the mode amplitude given by (4.20 a, b) becomes more complex. Some typical trajectories of A in the complex plane are shown in Fig. 9 for different values of the parameter η. If nonlinear effects are small which correspond to η large (or Re small compared to $\varepsilon^{-4/3}$), the amplitudes of the Kelvin mode A and geostrophic mode A_0 converge toward a fixed point. This fixed point is easily obtained by equating the time-derivative in (4.20 a, b) to zero. It is worth pointing out that the first effect of nonlinearities is to detune the Kelvin mode. Indeed the terms originating from the nonlinear interaction of the mode with itself and with the geostrophic mode are both expressed as a real number multiplying iA. This form is identical to that of the detuning term i$Af/(\varepsilon^{2/3} a_i)$ and the viscous detuning term $-\eta \operatorname{Im}(\mu)iA$.

For larger values of the Reynolds number (or smaller values of η), the fixed point may become unstable. In this case, the trajectory of A in the complex plane converges toward a limit cycle as shown on Fig. 9. However, this cycle could not be observed experimentally because it corresponds to experimental parameters leading to instability as shown in the next section.

As noted by Gans (1970) in the viscous regime, the resonances are important when the amplitude at the resonance (of the order of $\epsilon \sqrt{Re} f/\mu$ in the viscous regime) is much larger than the linear amplitude (of the order of ϵ) outside of the resonance. Since the term f/μ decreases with the radial wavenumber δ as $\delta^{-7/2}$, we recover that the resonances are visible if $\delta < Re^{1/7}$ in the viscous regime. Doing the same analysis in the non linear regime, the resonance is visible only if the amplitude at the resonance, which scales as $(\epsilon f/\sigma)^{1/3}$ is larger than the linear amplitude ϵ outside of the resonance. Since f/σ scales as $\delta^{-11/2}$, we find that the resonance is important when $\delta < \epsilon^{-4/11}$. In the general case, the resonances are thus visible if the radial wavenumber δ is smaller than these two bounds scaling as $Re^{1/7}$ and $\epsilon^{-4/11}$ respectively.

4.2.2. *Experimental amplitude at the resonance*

Figure 10 shows the experimental measurement of the amplitude of the first Kelvin mode at its second resonance for three different Reynolds numbers. For small Reynolds numbers, the temporal evolution of the amplitude is exponential $A_f(1 - e^{-t/t_s})$, with a final amplitude A_f and a settling time t_s which can be easily obtained by a least-square fit. However, for higher Reynolds numbers, the amplitude strongly oscillates before reaching a quasi-stationary final amplitude. This may be due to the nonlinear effects (which create a decaying oscillation of the amplitude), but in fact it mostly comes from the onset of a three-dimensional instability which is slowly growing during the transient stage. This oscillation prevents the correct determination of the final amplitude and introduces a large error, which is taken as the difference between the maximum and the local minimum of the amplitude. This error is shown in the next figures as error bars on the amplitude.

To clearly demonstrate that the flow has become three-dimensionally unstable at high

Reynolds numbers, we have plotted in Fig. 11(a) the instantaneous vorticity field found in the cylinder for the second resonance of the first Kelvin mode. The vorticity is made of several small vortices, which completely hide the organised structure of the initial Kelvin mode. However, this Kelvin mode is recovered (at a smaller amplitude) when plotting the mean vorticity field calculated on 100 fields (i.e. during 50 rotation periods), as in Fig. 11(b). It is striking to see that although the flow seems completely turbulent, the resonant Kelvin mode is still present with an amplitude only slightly oscillating in time. In this case, the current nonlinear theory cannot apply anymore because other Kelvin modes have appeared because of an instability.

By plotting the transient regimes for each frequency ω, we were able to measure the final amplitude A decomposed on its norm $|A|$ and argument α such that $A = |A|\mathrm{e}^{\mathrm{i}\alpha}$. They are plotted in Fig. 12 as a function of the dimensionless frequency ω around the second resonance of the first Kelvin mode and for $\eta = 0.22$. This solution is compared to the theoretical viscous solutions (linear and nonlinear). What is intended here by viscous linear (respectively nonlinear) theory is the set of equations (4.20 a, b) in the limit $\eta \gg 1$ [respectively for $\eta = O(1)$]. Despite the large error bars, the comparison between experiment and theory clearly shows that both nonlinear and viscous effects are needed to predict the correct amplitude of the mode. The viscous effects saturate the amplitude of the mode at a finite value, and the nonlinear effects shift the maximum of the peak toward smaller frequencies ω. The overall agreement is excellent for the amplitude. However, the experimental determination of the orientation of the mode α is closer to the linear theory than to the nonlinear theory. This discrepancy may come from transient effects: the measurements can only be done during a small duration, due to the presence of an instability. When looking at the solid line of Fig. 9, we can understand that the amplitude might be correctly predicted although the argument is not at its final value.

4.2.3. *Scaling at the resonance*

Five series of experiments were conducted to study the dependence of the amplitude with the Reynolds number when the frequency ω is exactly equal to the resonant frequency $\omega_{i,n}$. For this purpose, Ω_1 and Ω_2 were varied in each experiment, by keeping a fixed dimensionless frequency ω. It has been done for the first three resonances of the first Kelvin mode and for the first two resonances of the second Kelvin mode. Figure 13 shows the final amplitude of the mode after the transient stage. The results are in excellent agreement with the present theoretical predictions, knowing that there are no fitting parameters. They clearly show that the amplitude scales with $Re^{1/2}$ at low Reynolds numbers and saturates due to nonlinear effects at large Reynolds numbers. This saturation value decreases rapidly with the number of the resonance n. There is a large uncertainty in the nonlinear regime because of the onset of the three-dimensional instability as discussed above, which makes the validation of the nonlinear saturation more difficult. However, there is an agreement up to 50%. It can be noted that the exact theory given by (4.14) and (4.17) and plotted as thin lines is very close to the approximate theory given by (4.20a,b) plotted as thick lines: this means that it is justified to neglect the volume viscous damping of the geostrophic modes in the regime we have studied.

The dimensionless settling time t_s measured during the transient response is also plotted for these resonances in Fig. 14 as a function of the Reynolds number. It is compared to the viscous time $Re/(Re^{1/2}\mu + \nu)$. Although there is a large scatter, the agreement seems to be good. The settling time is only measured in the viscous regime since it is impossible to determine the settling time in the nonlinear regime when the transient response is not exponential anymore (as shown in Fig. 10).

Figure 15 shows the argument α of the complex amplitude as a function of the Reynolds number for the same five resonances. At low Reynolds numbers, the angles are determined by the viscous theory and are equal to $\pm 90°$ (if viscous detuning are neglected). It means that, at the resonance, the mode is perpendicular to its direction in the linear inviscid theory (or far from the resonances). However, when the nonlinear effects become large, the phase shift occurs at a frequency different from $\omega_{i,n}$, and the angle is thus equal to $0°$ or $180°$ at $\omega = \omega_{i,n}$. The agreement with the experimental results is correct for the first resonance of the first mode. However, there is a large scatter for the other resonances, and it is hard to ensure the validity of the theoretical predictions.

Finally, we have measured the dependence of the amplitude A with the small parameter ε by varying the precession angle from 0.5 to $10°$. The measured amplitudes are plotted in Fig. 16 and compared to the theoretical predictions. We recover that the amplitude scales as $\varepsilon^{2/3}$ in the viscous regime and then saturates at a fixed value for large precession angles. The agreement is again excellent in the viscous regime and fairly good in the nonlinear regime although the theory slightly overestimates the amplitude. This might be due once again to the appearance of a three-dimensional instability before the final amplitude has been reached. This relative discrepancy could be also due to the fact that the theoretical derivation assumes that $\varepsilon^{1/3}$ is asymptotically small whereas it goes up to 0.5 when the precession angle is large.

4.2.4. *Geostrophic modes*

As was previously stated in §4.2.1, the nonlinear and viscous effects leed to the generation of a geostrophic mode. This mode is mainly responsible for the saturation of the mode amplitude since the parameter ξ is generally larger than the parameter σ in (4.20 a) as it appears in tables 1 and 2. It is thus essential to check if the theory predicts an accurate amplitude of the geostrophic mode. Figure 17 shows the velocity profile of the geostrophic mode for the first and second modes. It has been obtained by taking an azimuthal average of the azimuthal velocity (this way, the velocity of the Kelvin modes are conveniently removed). For the first mode, the measured profile is bell-shaped and depends very weakly on the Reynolds number. This is in excellent agreement with the nonlinear theory. For the second Kelvin mode, the geostrophic profile is more complex. It exhibits two velocity maxima, but still vanishes for $r = 1$. This is due to the simultaneous presence of several components $J_1(d_j r)$ in the geostrophic mode. It is again in fairly good agreement with the nonlinear theory, although the minimum is less pronounced in the experiments.

It is possible to decompose these profiles on the Bessel functions $J_1(d_j r)$ (d_j being the roots of the bessel function) in order to get the amplitudes A_0^j of the geostrophic mode as defined in (4.8) and (4.9). For the first Kelvin mode, the amplitude A_0^1 is much larger than the others since the geostrophic mode is mostly bell-shaped. We have thus plotted this amplitude A_0^1 as a function of the Reynolds number and the parameter ε. In the viscous regime, the amplitude A_0^1 roughly scales as the Reynolds number and as $\varepsilon^{4/3}$, since it scales as the square of the amplitude A. This means that the total geostrophic motion $A_0 \varepsilon^{2/3} v_0$ scales as the square of the forcing parameter ε. It can be noted that there are some small variations of the scaling exponent among the resonances, which are due to the volumic diffusion terms $d_j^2 Re^{-1/2}$. In the nonlinear regime, the geostrophic amplitude A_0^1 saturates because the amplitude A also saturates. This means that the geostrophic motion scales as $\varepsilon^{2/3}$ in this regime. The agreement between the experiment and the theory is good for the first two resonances: the scaling exponents and the multiplication factors are correct, although the theory slightly overestimates the amplitude of the first mode in the nonlinear regime. For the third resonance, the amplitude is much smaller

in the experiments than in the theory, but the velocity of the geostrophic mode is very small in this case and the uncertainty is thus very high.

For the second Kelvin mode, the geostrophic profile contains more than one component and we thus need to plot the amplitudes A_0^j, j varying from 1 to 3. They are plotted in Fig. 19 and compared to the theory. It is surprising to see that here, the theory underestimates the amplitudes by a factor 10. Again this discrepancy could be due to the fact that $\varepsilon^{1/3}$ is not very small and thus the asymptotic decomposition may not be valid anymore in this case.

5. Conclusion

In this paper we addressed both experimentally and theoretically the flow inside a rotating cylinder subject to a weak precession. We have shown that this flow can be expressed as a sum of Kelvin modes which have been measured for the first time using Particle Image Velocimetry. We have distinguished two cases depending on the precession frequency. When this forcing frequency is not equal to a natural frequency of a Kelvin mode, the flow is said to be non-resonant and a linear inviscid theory can predict accurately the amplitude of the forced Kelvin modes in the limit of small precession amplitude and large Reynolds number. However, if the forcing frequency is resonant, this linear inviscid theory is unable to give the mode amplitude since it diverges. In this case, a viscous and nonlinear theory has been introduced to predict the finite value of the mode amplitude.

In the resonant case, there are two different regimes depending on the value of the Reynolds number. For small enough Reynolds numbers, nonlinear effects are negligible and taking into account the effects of both the viscous boundary layers and the volume viscous damping is enough to predict the dynamics of the resonant Kelvin mode as it has already been shown by Gans (1970) in the particular case of a precession angle of 90°. It yields a saturation of the mode amplitude which scales as $Re^{1/2}$ in excellent agreement with the experimental results.

For larger Reynolds numbers, weakly nonlinear effects have to be taken into account together with viscous effects. It leads to the saturation of the mode amplitude at a value which scales as $\theta^{1/3}$, where θ is the precession angle supposedly small. It is thus independent of the Reynolds number. This scaling is correctly recovered experimentally. An interesting point is that experiments show the presence of a geostrophic motion, whose amplitude always scales as the square of the Kelvin mode amplitude, as can be predicted by the nonlinear and viscous theory. This small geostrophic motion has been observed and measured in the experiments and its amplitude has been shown to be correctly predicted by the theory for the first Kelvin mode.

In the present paper, we have characterised the stable flow inside a precessing cylinder in all regimes. In the future, these results can serve as a basis for a stability study of this flow. Indeed, it is known from McEwan (1970) and Manasseh (1992) that Kelvin modes can become unstable and even turbulent for large Reynolds numbers. Such a breakdown of the flow has been observed in our experiments, and always appeared at the transition between the viscous and the nonlinear regime, i.e. when the nonlinear effects cease to be negligible. The instability of the Kelvin modes is probably due to a triadic resonance similarly to the elliptic instability (Kerswell 2002; Eloy *et al.* 2003). A theoretical and experimental study is currently carried out to understand this instability better.

Finally, it would be interesting to know if the present theoretical framework can hold when the flow becomes unstable and eventually turbulent. Indeed, the Kelvin modes are still excited in this case, although they are hidden by the presence of a very disordered

flow (which can still be expressed as a sum of Kelvin modes). This would have great consequences for industrial and geophysical applications for which the Reynolds numbers are usually a few decades higher than in the laboratory experiments.

Appendix A. Four-component formulation

The operators appearing in equation (2.8) are defined by

$$\mathcal{I} = \begin{pmatrix} 1 & 0 & 0 & 0 \\ 0 & 1 & 0 & 0 \\ 0 & 0 & 1 & 0 \\ 0 & 0 & 0 & 0 \end{pmatrix}, \tag{A 1}$$

$$\mathcal{D} = \begin{pmatrix} 0 & 0 & -\mathrm{i} & 0 \\ 0 & 0 & 1 & 0 \\ \mathrm{i} & -1 & 0 & 0 \\ 0 & 0 & 0 & 0 \end{pmatrix}, \tag{A 2}$$

$$\mathcal{L} = \begin{pmatrix} \Delta - \dfrac{1}{r^2} & -\dfrac{2}{r^2}\dfrac{\partial}{\partial\varphi} & 0 & 0 \\ \dfrac{2}{r^2}\dfrac{\partial}{\partial\varphi} & \Delta - \dfrac{1}{r^2} & 0 & 0 \\ 0 & 0 & \Delta & 0 \\ 0 & 0 & 0 & 0 \end{pmatrix}, \tag{A 3}$$

where

$$\Delta = \frac{1}{r}\frac{\partial}{\partial r} + \frac{\partial^2}{\partial r^2}\frac{1}{r^2}\frac{\partial^2}{\partial\varphi^2} + \frac{\partial}{\partial z^2} \tag{A 4}$$

and

$$\mathcal{M} = \begin{pmatrix} 0 & -2 & 0 & \dfrac{\partial}{\partial r} \\ 2 & 0 & 0 & \dfrac{1}{r}\dfrac{\partial}{\partial\varphi} \\ 0 & 0 & 0 & \dfrac{\partial}{\partial z} \\ \dfrac{\partial}{\partial r} + \dfrac{1}{r} & \dfrac{1}{r}\dfrac{\partial}{\partial\varphi} & \dfrac{\partial}{\partial z} & 0 \end{pmatrix}. \tag{A 5}$$

The vectors $\mathbf{F}_0$ and $\mathbf{N}(\mathbf{v}_1, \mathbf{v}_2)$ are defined by

$$\mathbf{F}_0 = \begin{pmatrix} 0 \\ 0 \\ -r\omega \\ 0 \end{pmatrix}, \tag{A 6}$$

and

$$\mathbf{N}(\mathbf{v}_1, \mathbf{v}_2) = \begin{pmatrix} \mathbf{u}_1 \times (\boldsymbol{\nabla} \times \mathbf{u}_2) + \overline{\mathbf{u}}_1 \times (\boldsymbol{\nabla} \times \mathbf{u}_2) \\ 0 \end{pmatrix}. \tag{A 7}$$

Appendix B. Extraction of the mode amplitude a_i

The PIV measurements give the two components $\mathbf{u}_{\text{exp}} = (u_{\text{exp}}, v_{\text{exp}})$ of the (real) transverse velocity field at a specific height z. We want to obtain the amplitudes a_i and the tilt angles α_i of the first 5 Kelvin modes whose transverse components are given in the reference frame of the rotating platform by $\mathbf{u}_i(r, \varphi, z) = \mathrm{e}^{\mathrm{i}\varphi}(u_i, v_i) \sin(k_i z)$, ($u_i$ and v_i being given in Eq. (3.5)). We thus suppose that the experimental velocity field is given by

$$\mathbf{u}_{\text{exp}}(r, \varphi, z) = \sum_i a_i \begin{pmatrix} -\mathrm{i} \sin(\varphi + \alpha_i) u_i(r) \\ \cos(\varphi + \alpha_i) v_i(r) \end{pmatrix}. \tag{B 1}$$

It can be noted that $\mathbf{u}_{\text{exp}}$ is real since u_i is purely imaginary and v_i is purely real.

We introduce the scalar product $\langle \mathbf{X} | \mathbf{Y} \rangle = \int_0^{2\pi} \int_0^{0.9} (\overline{X}_r Y_r + \overline{X}_\varphi Y_\varphi) \, r \, \mathrm{d}r \, \mathrm{d}\varphi$ for which the Kelvin modes are almost orthogonal: they would be orthogonal if the integration was achieved over the whole section $0 < r < 1$. If we define the complex experimental velocity (which can be easily derived numerically)

$$\mathbf{u}_{\text{exp}}^c(r, \varphi, z) = \mathbf{u}_{\text{exp}}(r, \varphi, z) - \mathrm{i} \, \mathbf{u}_{\text{exp}}(r, \varphi + \pi/2, z) \tag{B 2}$$

we find that the scalar product $\langle \mathbf{u}_i | \mathbf{u}_{\text{exp}}^c \rangle$ is equal to:

$$\langle \mathbf{u}_i | \mathbf{u}_{\text{exp}}^c \rangle = \sum_j M_{ij} a_j \mathrm{e}^{\mathrm{i}\alpha_j} \sin(k_j z) \tag{B 3}$$

where $M_{ij} = 2\pi \int_0^{0.9} (\overline{u_i} u_j + \overline{v_i} v_j) r \, \mathrm{d}r$. If we consider only the five first Kelvin modes, we can invert numerically the 5×5 matrix M to get:

$$\left(a_i \mathrm{e}^{\mathrm{i}\alpha_i} \sin(k_i z) \right)_{i=1,5} = M^{-1} \left(\langle \mathbf{u}_i | \mathbf{u}_{\text{exp}}^c \rangle \right)_{i=1,5}. \tag{B 4}$$

The tilt angles α_i of the Kelvin modes are thus equal to the argument of this expression and the amplitudes a_i to the modulus of this expression divided by $(\sin(k_i z))_{i=1,5}$.

Appendix C. Calculation of the nonlinear coefficients

The aim of this Appendix is to calculate the coefficients f, σ and ξ_j appearing in the nonlinear amplitude equation (4.14).

C.1. *Order $\varepsilon^{2/3}$*

At order $\varepsilon^{2/3}$, the particular solution of (4.7) is given by (4.8) where

$$\mathbf{v}_{2k} = \begin{pmatrix} 0 \\ a_{2k} \cos(2k_i z) \\ 0 \\ p_{2k} \cos(2k_i z) \end{pmatrix}, \quad \mathbf{v}_{2\omega} = \begin{pmatrix} \dfrac{\mathrm{i}}{r} a_{2\omega} \\ -\dfrac{1}{2} \dfrac{\mathrm{d}a_{2\omega}}{\mathrm{d}r} \\ 0 \\ p_{2\omega} \end{pmatrix}, \tag{C 1a,b}$$

with

$$a_{2k} = \frac{\mathrm{i}k_i}{\omega} \left(v_i w_i - \frac{1}{2k_i} \frac{\partial(u_i v_i)}{\partial r} \right), \quad a_{2\omega} = \frac{\omega \delta_i^2}{(\omega^2 - 4)^2} \left[J_1^2(\delta_i r) - J_1^2(\delta_i) \, r^2 \right]. \tag{C 2a,b}$$

C.2. *Order* ε

We first need to calculate the scalar product N, which is the norm of the velocity field

$$N = \mathbf{v}_i \odot \mathcal{I}\, \mathbf{v}_i = 2\pi h \frac{\omega^2 \left(\omega + 2\delta_i^2 - 2 \right) - 4\omega + 8}{\omega^2 \left(4 - \omega^2 \right)^2} J_1^2(\delta_i)$$

$$+ \frac{\pi}{k_i} \sin(k_i h) \frac{\omega^2 \left(\omega - \delta_i^2 \omega - 2 \right) - 4\omega + 8}{\omega^2 \left(4 - \omega^2 \right)^2} J_1^2(\delta_i). \tag{C 3}$$

It can be noted that the last term vanishes at the resonance. The term of forcing comes from

$$F = \mathbf{v}_i\, \mathrm{e}^{\mathrm{i}(\omega t + \varphi)} \odot \zeta\, \mathbf{F}_0 \mathrm{e}^{\mathrm{i}(\omega t + \varphi)} = 2\pi\zeta \frac{2\mathrm{i}}{\delta_i^2} \frac{\omega + 2}{\omega} \sin\left(\frac{k_i h}{2} \right) J_1(\delta_i), \tag{C 4}$$

which is a pure imaginary number. The coefficient of forcing f appearing in the amplitude equation (4.14) is simply

$$f = \frac{F}{\mathrm{i}N}, \tag{C 5}$$

where N and F are given by (C 3) and (C 4).

The coefficient σ in (4.14) is separated in two parts. The first one comes from the nonlinear interaction of $\mathbf{V}_1$ with $\mathbf{v}_{2k}$

$$\sigma_{2k} = \mathbf{v}_i\, \mathrm{e}^{\mathrm{i}(\omega t + \varphi)} \odot \left[\mathbf{N}\left(\mathbf{v}_{2k}, \mathbf{v}_i\, \mathrm{e}^{\mathrm{i}(\omega t + \varphi)} \right) + \mathbf{N}\left(\mathbf{v}_i\, \mathrm{e}^{\mathrm{i}(\omega t + \varphi)}, \mathbf{v}_{2k} \right) \right], \tag{C 6a}$$

$$= 2\pi h \int_0^1 \left(2k_i\, a_{2k}\, v_i w_i - a_{2k} \frac{\partial (u_i v_i)}{\partial r} \right) r \mathrm{d}r, \tag{C 6b}$$

with a_{2k} given by (C 2a). The other term comes from the interaction of $\mathbf{V}_1$ with $\mathbf{v}_{2\omega}$

$$\sigma_{2\omega} = \mathbf{v}_i\, \mathrm{e}^{\mathrm{i}(\omega t + \varphi)} \odot \mathbf{N}\left(\mathbf{v}_{2\omega} \mathrm{e}^{2\mathrm{i}(\omega t + \varphi)}, \overline{\mathbf{v}_i}\, \mathrm{e}^{-\mathrm{i}(\omega t + \varphi)} \right), \tag{C 7a}$$

$$= 2\pi h \frac{\mathrm{i}k_i}{\omega} \int_0^1 \left(\frac{\mathrm{d}a_{2\omega}}{\mathrm{d}r} u_i w_i - \frac{2\mathrm{i}a_{2\omega}}{r} v_i w_i \right) r \mathrm{d}r, \tag{C 7b}$$

where the term associated with $\mathbf{N}(\mathbf{v}_i, \mathbf{v}_{2\omega})$ has been omitted because its scalar product with $\mathbf{v}_i\, \mathrm{e}^{\mathrm{i}(\omega t + \varphi)}$ is zero. The final coefficient σ used in the amplitude equation (4.14) is

$$\sigma = \frac{\sigma_{2k} + \sigma_{2\omega}}{\mathrm{i}N}, \tag{C 8}$$

where N, σ_{2k} and $\sigma_{2\omega}$ are given by (C 3), (C 6b) and (C 7b). The integrals appearing in the coefficients σ_{2k} and $\sigma_{2\omega}$ can be evaluated numerically. It is easy to see that σ_{2k} and $\sigma_{2\omega}$ are pure imaginary and therefore σ is real.

Finally the coefficients ξ_j describe the nonlinear interaction of the Kelvin mode with the j-th geostrophic mode

$$X_j = \mathbf{v}_i\, \mathrm{e}^{\mathrm{i}(\omega t + \varphi)} \odot \left[\mathbf{N}\left(\mathbf{v}_0^j, \mathbf{v}_i\, \mathrm{e}^{\mathrm{i}(\omega t + \varphi)} \right) + \mathbf{N}\left(\mathbf{v}_i\, \mathrm{e}^{\mathrm{i}(\omega t + \varphi)}, \mathbf{v}_0^j \right) \right], \tag{C 9a}$$

$$= -2\pi h \int_0^1 \left(\frac{2\mathrm{i}k_i}{\omega} v_0^j u_i w_i + \frac{1}{r} \frac{\mathrm{d}(r v_0^j)}{\mathrm{d}r} u_i v_i \right) r \mathrm{d}r, \tag{C 9b}$$

where v_0^j is given by (4.9). The coefficient ξ_j of (4.14) is

$$\xi_j = -\frac{X_j}{\mathrm{i}N}, \tag{C 10}$$

where N and X_j are given by (C 3) and (C 9b). Again, the integral in (C 9b) is calculated numerically.

Some numerical values of the coefficients f, σ and ξ_j whose analytical expressions are given by (C 5), (C 8) and (C 10) are found in tables 1, 2 and 3.

Appendix D. Linear viscous boundary layers (Ekman pumping)

In this appendix we derive the viscous correction to the main flow $\mathbf{V}$ in the boundary layers. This correction can be written as

$$\widetilde{\mathbf{V}} = \varepsilon^{1/3} A \left(\widetilde{\mathbf{v}}_i + Re^{-1/2}\, \widetilde{\mathbf{v}}_3 \right) \mathrm{e}^{\mathrm{i}(\omega t + \varphi)} + \text{o.t.}, \tag{D 1}$$

with the boundary conditions $\mathbf{V} + \widetilde{\mathbf{V}} = 0$ on the walls and $\widetilde{\mathbf{V}}$ tends to zero far from the walls. In the previous expression, $\widetilde{\mathbf{v}}_i = (\widetilde{u}_i, \widetilde{v}_i, \widetilde{w}_i, \widetilde{p}_i)$ and $\widetilde{\mathbf{v}}_3 = (\widetilde{u}_3, \widetilde{v}_3, \widetilde{w}_3, \widetilde{p}_3)$ are of order 1. The added corrective flow (Ekman pumping) is denoted $\widetilde{\mathbf{v}}_3$ because, as we shall see below, this flow constitutes the normal boundary condition for the bulk flow $\mathbf{V}_3$ at order ε. This calculation is classical and can be found in several sources (e.g. Greenspan 1968; Gans 1970).

D.1. *Lateral wall*

At first, let us focus on the lateral wall $r = 1$. By taking into account the viscous effects in (2.8) and considering the rescaled coordinate

$$\widetilde{r} = Re^{-1/2}\, (1 - r), \tag{D 2}$$

one can write the linear Navier-Stokes equation valid close to the lateral wall

$$\left(\mathrm{i}\omega \mathcal{I} - Re^{1/2}\, \frac{\partial}{\partial \widetilde{r}} \mathcal{R}_l + \mathcal{M}_l - \frac{\partial^2}{\partial \widetilde{r}^2} \mathcal{I} \right) \widetilde{\mathbf{V}} = O\left(Re^{-1} \widetilde{\mathbf{V}} \right), \tag{D 3}$$

where the tensors $\mathcal{R}_l$ et $\mathcal{M}_l$ are defined as follow

$$\mathcal{R}_l = \begin{pmatrix} 0 & 0 & 0 & 1 \\ 0 & 0 & 0 & 0 \\ 0 & 0 & 0 & 0 \\ 1 & 0 & 0 & 0 \end{pmatrix} \quad \text{and} \quad \mathcal{M}_l = \begin{pmatrix} 0 & -2 & 0 & 0 \\ 2 & 0 & 0 & \mathrm{i} \\ 0 & 0 & 0 & \dfrac{\partial}{\partial z} \\ 1 & \mathrm{i} & \dfrac{\partial}{\partial z} & 0 \end{pmatrix}. \tag{D 4}$$

At order $Re^{1/2}$, one gets

$$\frac{\partial}{\partial \widetilde{r}}(\mathcal{R}_l\, \widetilde{\mathbf{v}}_i) = \mathbf{0}, \tag{D 5}$$

which leads to $\widetilde{u}_i = \widetilde{p}_i = 0$.

At order 1, (D 3) gives

$$\frac{\partial}{\partial \widetilde{r}}(\mathcal{R}_l\, \widetilde{\mathbf{v}}_3) = \left(\mathrm{i}\omega \mathcal{I} + \mathcal{M}_l - \frac{\partial^2}{\partial \widetilde{r}^2} \mathcal{I} \right) \widetilde{\mathbf{v}}_i. \tag{D 6}$$

The solution of this linear system with the boundary conditions $\mathbf{v}_i + \widetilde{\mathbf{v}}_i = 0$ in $\widetilde{r} = 0$ and $\widetilde{\mathbf{v}}_i$ vanishes to zero for $\widetilde{r} \gg 1$ is

$$\widetilde{v}_i(\widetilde{r}, z) = -v_i(1) \sin(k_i z)\, \mathrm{e}^{-\kappa \widetilde{r}} \quad \text{and} \quad \widetilde{w}_i(\widetilde{r}, z) = -w_i(1) \cos(k_i z)\, \mathrm{e}^{-\kappa \widetilde{r}} \tag{D 7}$$

where κ is given by

$$\kappa = \frac{1+\mathrm{i}}{\sqrt{2}}\sqrt{\omega}. \tag{D 8}$$

and

$$\widetilde{u}_3 = \widetilde{\mathbf{v}}_3 \cdot \mathbf{n} = -\alpha_i\, J_1(\delta_i)\, \sin k_i z, \quad \text{in } r = 1, \tag{D 9}$$

where

$$\alpha_i = \frac{1+\mathrm{i}}{\sqrt{2}}\frac{(\delta_i^2 - 1)\,\omega^2 + 4}{(4 - \omega^2)\,\omega^{3/2}}. \tag{D 10}$$

D.2. *End walls*

An equivalent derivation can be done for the upper wall (the flow in the lower wall boundary layer is formally identical). Using the local rescaled coordinate

$$\widetilde{z} = Re^{1/2}\left(\frac{h}{2} - z\right), \tag{D 11}$$

one can rewrite the Navier-Stokes equation valid close to the upper wall

$$\left(\mathrm{i}\omega\mathcal{I} - Re^{1/2}\frac{\partial}{\partial\widetilde{z}}\mathcal{R}_u + \mathcal{M}_u - \frac{\partial^2}{\partial\widetilde{z}^2}\mathcal{I}\right)\widetilde{\mathbf{V}} = O\left(Re^{-1}\widetilde{\mathbf{V}}\right), \tag{D 12}$$

where the tensors $\mathcal{R}_u$ et $\mathcal{M}_u$ are defined as follow

$$\mathcal{R}_u = \begin{pmatrix} 0 & 0 & 0 & 0 \\ 0 & 0 & 0 & 0 \\ 0 & 0 & 0 & 1 \\ 0 & 0 & 1 & 0 \end{pmatrix} \quad \text{and} \quad \mathcal{M}_u = \begin{pmatrix} 0 & -2 & 0 & \dfrac{\partial}{\partial r} \\ 2 & 0 & 0 & \dfrac{\mathrm{i}}{r} \\ 0 & 0 & 0 & 0 \\ \dfrac{1}{r} + \dfrac{\partial}{\partial r} & \dfrac{\mathrm{i}}{r} & 0 & 0 \end{pmatrix}. \tag{D 13}$$

At order $Re^{1/2}$, one finds $\widetilde{w}_i = \widetilde{p}_i = 0$. At order 1, the projection of (D 12) onto the radial, azimuthal and pressure directions with the proper boundary conditions gives

$$\widetilde{u}_i(r,\widetilde{z}) = \mathrm{i}\,S(r)\,\mathrm{e}^{-\kappa_s\widetilde{z}} - \mathrm{i}\,D(r)\,\mathrm{e}^{-\kappa_d\widetilde{z}}, \tag{D 14a}$$

$$\widetilde{v}_i(r,\widetilde{z}) = S(r)\,\mathrm{e}^{-\kappa_s\widetilde{z}} + D(r)\,\mathrm{e}^{-\kappa_d\widetilde{z}}, \tag{D 14b}$$

where κ_s and κ_d are given by

$$\kappa_s = \frac{1+\mathrm{i}}{\sqrt{2}}\sqrt{\omega + 2}, \quad \text{and} \quad \kappa_d = \frac{1-\mathrm{i}}{\sqrt{2}}\sqrt{2 - \omega}, \tag{D 15}$$

and where S and D are given by

$$S(r) = \frac{\mathrm{i}\,u_i - v_i}{2}\sin(k_i h/2), \quad \text{and} \quad D(r) = \frac{-\mathrm{i}\,u_i - v_i}{2}\sin(k_i h/2). \tag{D 16}$$

The projection of (D 12) on the vertical direction gives

$$\widetilde{w}_3 = \left(\frac{2\mathrm{i}S}{r} + \mathrm{i}\frac{\mathrm{d}S}{\mathrm{d}r}\right)\frac{\mathrm{e}^{-\kappa_s\widetilde{z}}}{\kappa_s} - \mathrm{i}\frac{\mathrm{d}D}{\mathrm{d}r}\frac{\mathrm{e}^{-\kappa_d\widetilde{z}}}{\kappa_d}, \tag{D 17}$$

such that

$$\widetilde{w}_3 = \widetilde{\mathbf{v}}_3 \cdot \mathbf{n} = -\beta_i\,\sin(k_i h/2)\,J_1(\delta_i r), \quad \text{in } \widetilde{z} = 0 \quad \text{i.e.} \quad z = h/2, \tag{D 18}$$

where

$$\beta_i = \frac{1-\mathrm{i}}{2\sqrt{2}}\delta_i^2 \left[\frac{1}{(2-\omega)^{3/2}} + \frac{\mathrm{i}}{(2+\omega)^{3/2}}\right]. \tag{D 19}$$

D.3. *Geostrophic flow*

For the geostrophic flow, the viscous flow in the end wall boundary layers can be calculated with a similar method as for the Kelvin mode in D.2. This viscous flow is of the form

$$\widetilde{\mathbf{V}} = \varepsilon^{2/3}\sum_{j=1}^{\infty} A_0^j(\tau)\left(\widetilde{\mathbf{v}}_0^j + Re^{-1/2}\widetilde{\mathbf{v}}_4^j\right) + \text{o.t.}, \tag{D 20}$$

where $\widetilde{\mathbf{v}}_0^j = (\widetilde{u}_0^j, \widetilde{v}_0^j, \widetilde{w}_0^j, \widetilde{p}_0^j)$. One finds $\widetilde{w}_0^j = \widetilde{p}_0^j = 0$ and

$$\widetilde{u}_0^j = \frac{\mathrm{i}}{2}v_0^j\left(-\mathrm{e}^{-\kappa_1\widetilde{z}} + \mathrm{e}^{-\kappa_2\widetilde{z}}\right), \quad \text{and} \quad \widetilde{v}_0^j = -\frac{1}{2}v_0^j\left(\mathrm{e}^{-\kappa_1\widetilde{z}} + \mathrm{e}^{-\kappa_2\widetilde{z}}\right), \tag{D 21}$$

where $\kappa_1 = 1 + \mathrm{i}$ and $\kappa_2 = 1 - \mathrm{i}$. This leads to

$$\widetilde{w}_4^j = \widetilde{\mathbf{v}}_4^j \cdot \mathbf{n} = \widetilde{w}_4^j = \frac{1}{2}\left(\frac{\mathrm{d}v_0^j}{\mathrm{d}r} + \frac{v_0^j}{r}\right), \quad \text{in } z = h/2. \tag{D 22}$$

D.4. *Viscous coefficients*

The surface viscous coefficients appearing in (4.14) and (4.17) can now be calculated. If the surface of the cylinder is separated into two parts $S = S_l + S_e$, where S_l is the lateral wall and S_e the end walls, we have

$$\mu_l = \int_{S_l} p_i \sin(k_i z)\,\widetilde{\mathbf{v}}_3 \cdot \mathbf{n}\,\mathrm{d}^2S = -\pi\left[h - \sin(k_i h)/k_i\right]\alpha_i J_1^2(\delta_i), \tag{D 23a}$$

$$\mu_e = \int_{S_e} p_i \sin(k_i z)\,\widetilde{\mathbf{v}}_3 \cdot \mathbf{n}\,\mathrm{d}^2S = -2\pi\beta_i\frac{(\delta_i^2 - 1)\omega^2 + 4}{\delta_i^2\omega^2}J_1^2(\delta_i)\sin^2\left(\frac{k_i h}{2}\right), \tag{D 23b}$$

where we have used the formulation of $\widetilde{\mathbf{v}}_3 \cdot \mathbf{n}$ found in (D 9) and (D 18). Now using the relation (4.15) the viscous coefficient μ used in (4.14) is simply

$$\mu = -\frac{\mu_l + \mu_e}{N}, \tag{D 24}$$

where N is given by (C 3).

For the geostrophic flow, we obtain by integrating by parts

$$\mu_0 = \int_{S_e} p_0^j\,\widetilde{\mathbf{v}}_4^j \cdot \mathbf{n}\,\mathrm{d}^2S = -4\pi\int_0^1 v_0^{j\,2}r\mathrm{d}r, \tag{D 25}$$

where we have used $\widetilde{\mathbf{v}}_4^j \cdot \mathbf{n}$ as given by (D 22) and

$$N_0 = \mathbf{v}_0^j \odot \mathcal{I}\,\mathbf{v}_0^j = 2\pi h\int_0^1 v_0^{j\,2}r\mathrm{d}r, \tag{D 26}$$

which leads to a surface viscous coefficient $\mu_0/N_0 = -2/h$ as it appears in the amplitude equation (4.17).

The volume viscous coefficient ν is simply

$$\nu = \frac{-\mathbf{v}_i \odot \mathcal{L}\,\mathbf{v}_i}{\mathbf{v}_i \odot \mathcal{I}\,\mathbf{v}_i} = (k_i^2 + \delta_i^2). \tag{D 27}$$

Some useful numerical values of the viscous coefficients μ and ν obtained through (D 24) and (D 27) are given in tables 1 and 2.

Appendix E. Nonlinear viscous boundary layers

To calculate the forcing of the geostrophic flow by the Kelvin mode, we need to perform a weakly nonlinear analysis in the end wall boundary layer. We choose to focus on the upper wall boundary layer $z = h/2$ (the calculation is symmetric for the bottom wall) using the rescaled vertical coordinate $\widetilde{z}$ as defined by (D 11). Taking into account the nonlinear effects and considering only the forcing of geostrophic modes of angular frequency $\omega = 0$, the Navier-Stokes equation reads

$$\left(-Re^{1/2}\frac{\partial}{\partial\widetilde{z}}\mathcal{R}_u + \mathcal{M}_u - \frac{\partial^2}{\partial\widetilde{z}^2}\mathcal{I}\right)\widetilde{\mathbf{V}} = \mathbf{N}_u(\widetilde{\mathbf{V}},\widetilde{\mathbf{V}}) + \mathbf{N}_u(\mathbf{V},\widetilde{\mathbf{V}}) + \mathbf{N}_u(\widetilde{\mathbf{V}},\mathbf{V}) + \text{o.t.}, \quad \text{(E 1)}$$

where the operators $\mathcal{R}_u$ and $\mathcal{M}_u$ are defined in (D 13) and $\mathbf{N}_u$ is similar to the bilinear function $\mathbf{N}$ defined in (C 3) but adapted to the rescaled variable $\widetilde{z}$.

We now need to evaluate the right hand side of the above equation at order $\varepsilon^{2/3}$ focusing on the geostrophic component (independent of t and ϕ). It leads to

$$\mathbf{N}_u(\widetilde{\mathbf{V}},\widetilde{\mathbf{V}}) = \varepsilon^{2/3}|A|^2 \begin{pmatrix} \gamma_1(r,\widetilde{z}) \\ \kappa_1(r,\widetilde{z}) \\ 0 \\ 0 \end{pmatrix} + \text{o.t.} + O(\varepsilon), \quad \text{(E 2)}$$

where

$$\gamma_1 = \overline{\widetilde{v}}_i\left(\frac{\widetilde{v}_i}{r} - \frac{\mathrm{i}}{r}\widetilde{u}_i\right) - \overline{\widetilde{u}}_i\frac{\partial\widetilde{u}_i}{\partial r} - \overline{\widetilde{w}}_3\frac{\partial\widetilde{u}_i}{\partial\widetilde{z}}, \quad \text{(E 3a)}$$

$$\kappa_1 = \overline{\widetilde{u}}_i\left(\frac{\widetilde{v}_i}{r} - \frac{\partial\widetilde{v}_i}{\partial r}\right) - \overline{\widetilde{v}}_i\frac{\mathrm{i}\widetilde{v}_i}{r} - \overline{\widetilde{w}}_3\frac{\partial\widetilde{v}_i}{\partial\widetilde{z}}, \quad \text{(E 3b)}$$

where $\widetilde{u}_i$ and $\widetilde{v}_i$ are given by (D 14 a,b) and $\widetilde{w}_3$ is given by (D 17). The other two terms are

$$\mathbf{N}_u(\mathbf{V},\widetilde{\mathbf{V}}) = \varepsilon^{2/3}|A|^2 \begin{pmatrix} \gamma_2(r,\widetilde{z}) \\ \kappa_2(r,\widetilde{z}) \\ 0 \\ 0 \end{pmatrix} + \text{o.t.} + O(\varepsilon), \quad \text{(E 4a)}$$

$$\mathbf{N}_u(\widetilde{\mathbf{V}},\mathbf{V}) = \varepsilon^{2/3}|A|^2 \begin{pmatrix} \gamma_3(r,\widetilde{z}) \\ \kappa_3(r,\widetilde{z}) \\ 0 \\ 0 \end{pmatrix} + \text{o.t.} + O(\varepsilon), \quad \text{(E 4b)}$$

where

$$\gamma_2 = \sin\frac{k_ih}{2}\left[v_i\left(-\frac{\mathrm{i}}{r}\widetilde{u}_i + \frac{\widetilde{v}_i}{r}\right) + u_i\frac{\partial\widetilde{u}_i}{\partial r} - \overline{w}_3\frac{\partial\widetilde{u}_i}{\partial\widetilde{z}} - k_i\widetilde{z}\,\overline{w}_i\frac{\partial\widetilde{u}_i}{\partial\widetilde{z}}\right], \quad \text{(E 5a)}$$

$$\kappa_2 = \sin\frac{k_ih}{2}\left[u_i\left(\frac{\widetilde{v}_i}{r} + \frac{\partial\widetilde{v}_i}{\partial r}\right) - \frac{\mathrm{i}}{r}v_i\widetilde{v}_i - \overline{w}_3\frac{\partial\widetilde{v}_i}{\partial\widetilde{z}} - k_i\widetilde{z}\,\overline{w}_i\frac{\partial\widetilde{v}_i}{\partial\widetilde{z}}\right], \quad \text{(E 5b)}$$

$$\gamma_3 = \sin\frac{k_ih}{2}\left[\widetilde{v}_i\left(-\frac{\mathrm{i}}{r}u_i + \frac{v_i}{r}\right) + \widetilde{u}_i\frac{\partial u_i}{\partial r}\right], \quad \text{(E 5c)}$$

$$\kappa_3 = \sin\frac{k_ih}{2}\left[-\widetilde{u}_i\left(\frac{v_i}{r} + \frac{\partial v_i}{\partial r}\right) + \frac{\mathrm{i}}{r}v_i\widetilde{v}_i\right], \quad \text{(E 5d)}$$

where $w_3 = -\widetilde{w}_3(\widetilde{z} = 0)$.

The solution of (E 1) forced by the right hand side is sought at order $\varepsilon^{2/3}$ of the form

$$\widetilde{\mathbf{V}} = \varepsilon^{2/3}|A|^2 \left(\widetilde{\mathbf{v}}_2^{\text{NL}} + Re^{-1/2}\,\widetilde{\mathbf{v}}_4^{\text{NL}} \right). \tag{E 6}$$

Examining (E 1) at order $\varepsilon^{2/3}Re^{1/2}$ leads to $\widetilde{w}_2^{\text{NL}} = \widetilde{p}_2^{\text{NL}} = 0$. At order $\varepsilon^{2/3}$, it leads to

$$\left(\frac{\partial^4}{\partial\widetilde{z}^4} + 4 \right) \widetilde{u}_2^{\text{NL}} = 2\left(\kappa_1 + \kappa_2 + \kappa_3 \right) - \frac{\partial^2}{\partial\widetilde{z}^2}\left(\gamma_1 + \gamma_2 + \gamma_3 \right), \tag{E 7a}$$

$$\widetilde{v}_2^{\text{NL}} = -\frac{1}{2}\left(\gamma_1 + \gamma_2 + \gamma_3 + \frac{\partial^2\widetilde{u}_2^{\text{NL}}}{\partial\widetilde{z}^2} \right). \tag{E 7b}$$

The solution of the above system is a sum of the particular solution of (E 7 *a*) and the solution of the homogeneous system of the form $\widetilde{u}_2^{\text{NL}} = a_1\exp(-1+\mathrm{i})\widetilde{z} + a_2\exp(-1-\mathrm{i})\widetilde{z}$. The particular solution is found with a symbolic calculation software where the coefficients a_1 and a_2 are adjusted to satisfy the boundary conditions $\widetilde{u}_2^{\text{NL}} = \widetilde{v}_2^{\text{NL}} = 0$ in $\widetilde{z} = 0$ (the boundary condition of vanishing $\widetilde{\mathbf{v}}_2^{\text{NL}}$ for $\widetilde{z} \gg 1$ is ensured by the selection of the vanishing exponential in the particular solution).

Taking (E 1) at order $\varepsilon^{2/3}$ also gives the form of the flow orthogonal to the wall at order $\varepsilon^{2/3}Re^{-1/2}$ which satisfies

$$\frac{\partial}{\partial\widetilde{z}}\widetilde{w}_4^{\text{NL}} = -\left(\frac{1}{r} + \frac{\partial}{\partial r} \right) \widetilde{u}_2^{\text{NL}}. \tag{E 8}$$

Once this is integrated, the normal flow is $\widetilde{\mathbf{v}}_4^{\text{NL}} \cdot \mathbf{n} = \widetilde{w}_4^{\text{NL}}(\widetilde{z} = 0)$. The coefficients χ_j needed for the amplitude equation (4.17) can now be obtained

$$\chi_j = \frac{4\pi}{N_0}\int_0^1 p_0^j \left(\widetilde{\mathbf{v}}_4^{\text{NL}} \cdot \mathbf{n} - \widetilde{w}_4^{\text{SB}} \right) r\mathrm{d}r + \text{c.c.}, \tag{E 9}$$

where N_0 is given by (D 26) and

$$\widetilde{w}_4^{\text{SB}} = \int_0^1 \widetilde{\mathbf{v}}_4^{\text{NL}} \cdot \mathbf{n}\, r\mathrm{d}r + \text{c.c.}, \tag{E 10}$$

corresponds to the flow associated with a modification of the solid body rotation frequency.

REFERENCES

AGRAWAL, B. N. 1993 Dynamics characteristics of liquid motion in partially filled tanks of a spinning spacecraft. *J. Guid. Control Dynam.* **16** (4), 636–640.

BAO, G. W. & PASCAL, M. 1997 Stability of a spinning liquid filled spacecraft. *Appl. Mech.* **67**, 407–421.

ELOY, C., LE GAL, P. & LE DIZÈS, S. 2000 Experimental study of the multipolar vortex instability. *Phys. Rev. Lett.* **85**, 3400–3403.

ELOY, C., LE GAL, P. & LE DIZÈS, S. 2003 Elliptic and triangular instabilities in rotating cylinders. *J. Fluid Mech.* **476**, 357–388.

FABRE, D., SIPP, D. & JACQUIN, L. 2006 Kelvin waves and the singular modes of the lamb–oseen vortex. *J. Fluid Mech.* **551** (10), 235–274.

FULTZ, D. 1959 A note on overstability and elastoid-inertia oscillations of kelvin, solberg and bjerknes. *J. Meteorol.* **16**, 199–208.

GANS, R. F. 1970 On the precession of a resonant cylinder. *J. Fluid Mech.* **476**, 865–872.

GANS, R. F. 1984 Dynamics of a near-resonant fluid-filled gyroscope. *AIAA J.* **22**, 1465–1471.

GARG, S. C., FURUNOTO, N. & VANYO, J. P. 1986 Spacecraft nutational instability prediction by energy dissipation measurments. *J. Guid.* **9** (3), 357–361.

GOTO, S., ISHII, N., KIDA, S. & NISHIOKA, M. 2007 Turbulence generator using a precessing sphere. *Phys. Fluids* **19**.

GREENSPAN, H. P. 1968 *The theory of rotating fluids*. Cambridge University Press.

GREENSPAN, H. P. 1969 On the non-linear interaction of inertial modes. *J. Fluid Mech.* **36** (2), 257–264.

KELVIN, L. 1880 Vibrations of a columnar vortex. *Phil. Mag.* **10**, 155–168.

KERSWELL, R. R. 1999 Secondary instabilities in rapidly rotating fluids: inertial wave breakdown. *J. Fluid Mech.* **382**, 283–306.

KERSWELL, R. R. 2002 Elliptical instability. *Ann. Rev. Fluid Mech.* **34**, 83–113.

KERSWELL, R. R. & BARENGHI, C. F. 1995 On the viscous decay rates of inertial waves in a rotating cylinder. *J. Fluid Mech.* **285**, 203–214.

KOBINE, J. J. 1995 Inertial wave dynamics in a rotating and precessing cylinder. *J. Fluid Mech.* **303**, 233–252.

KOBINE, J. J. 1996 Azimuthal flow associated with inertial wave resonance in a precessing cylinder. *J. Fluid Mech.* **319**, 387–406.

KUDLICK, M. 1966 On the transient motions in a contained rotating fluid. PhD thesis, Massachussets Institute of Technology.

LORENZANI, S. & TILGNER, A. 2001 Fluid instabilities in precessing spheroidal cavities. *J. Fluid Mech.* **447**, 111–128.

MAHALOV, A. 1993 The instability of rotating fluid columns subjected to a weak external coriolis-force. *Phys. Fluids A* **5** (4), 891–900.

MALKUS, W. V. R. 1989 An experimental study of global instabilities due to tidal (elliptical) distortion of a rotating elastic cylinder. *Geophys. Astrophys. Fluid Dynamics* **48**, 123–134.

MANASSEH, R. 1992 Breakdown regimes of inertia waves in a precessing cylinder. *J. Fluid Mech.* **243**, 261–296.

MASON, D. M. & KERSWELL, R. R. 1999 Nonlinear evolution of the elliptical instability: an example of inertial breakdown. *J. Fluid Mech.* **396**, 73–108.

MCEWAN, A. D. 1970 Inertial oscillations in a rotating fluid cylinder. *J. Fluid Mech.* **40** (3), 603–640.

MEUNIER, P. & LEWEKE, T. 2003 Analysis and minimization of errors due to high gradients in particule image velocimetry. *Exp. Fluids* **35** (5), 408–421.

NOIR, J., JAULT, D. & CARDIN, P. 2001 Numerical study of the motions within a slowly precessing sphere at low Ekman number. *J. Fluid Mech.* **437**, 283–29.

POINCARÉ, H. 1910 Sur la précession des corps déformables. *Bull. Astro.* **27**, 257–264.

RACZ, J.-P. & SCOTT, J. F. 2007 Parametric instability in a rotating cylinder of gas subject to sinusoidal axial compression. Part2. weakly nonlinear theory. *J. Fluid Mech.* **595**, 291–321.

SIPP, D. 2000 Weakly nonlinear saturation of short-wave instabilities in a strained lamb-oseen vortex. *Phys. Fluids* **12**, 1715–1729.

STEWARTSON, K. 1958 On the stability of a spinning top containing liquid. *J. Fluid Mech.* **5**, 577–592.

THOMPSON, R. 1970 Diurnal tides and shear instabilities in a rotating cylinder. *J. Fluid Mech.* **40**, 737–751.

VANYO, J. P. 1993 *Rotating fluids in engineering and science*. Dover, New York.

WALEFFE, F. 1989 The 3d instability of a strained vortex and its relation to turbulence. PhD thesis, Massachusetts Institute of Technology.

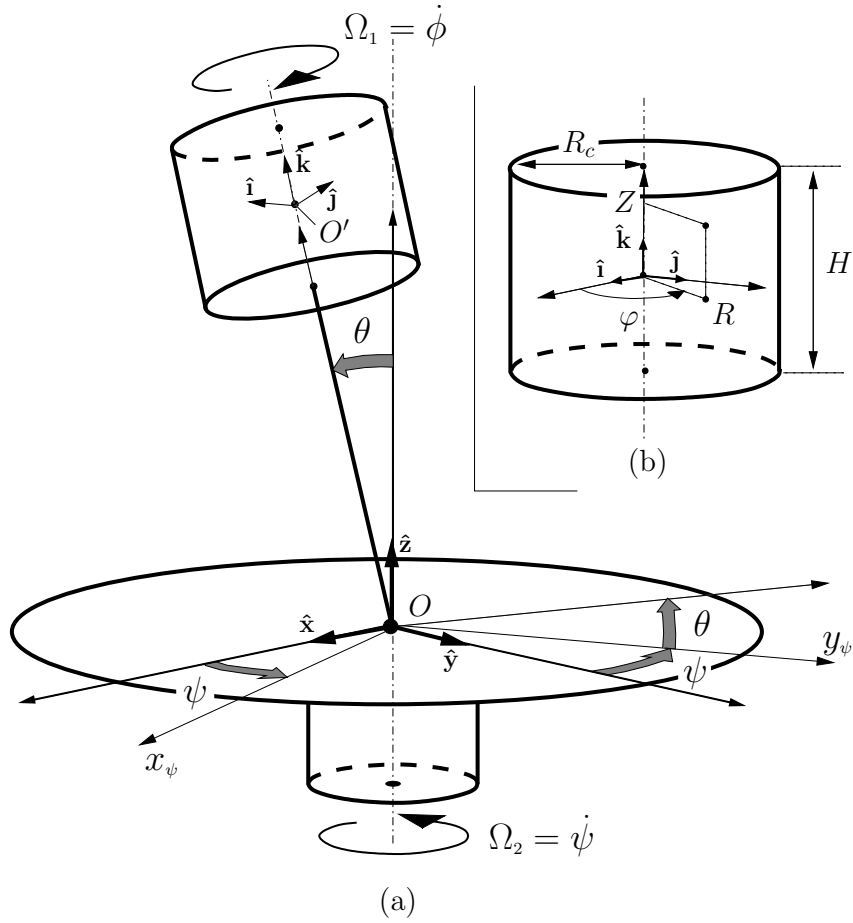WOOD, W. W. 1965 Properties of inviscid, recirculating flows. *J. Fluid Mech.* **22** (2), 337–346.

FIGURE 1. Sketch of the problem. (a) The cylinder of radius R_c and height H rotates about its axis at fixed angular frequency Ω_1. The precession rate Ω_2 and the nutation angle θ are also fixed. (b) Polar coordinates (R, φ, Z) defined in the cylinder rotating frame.
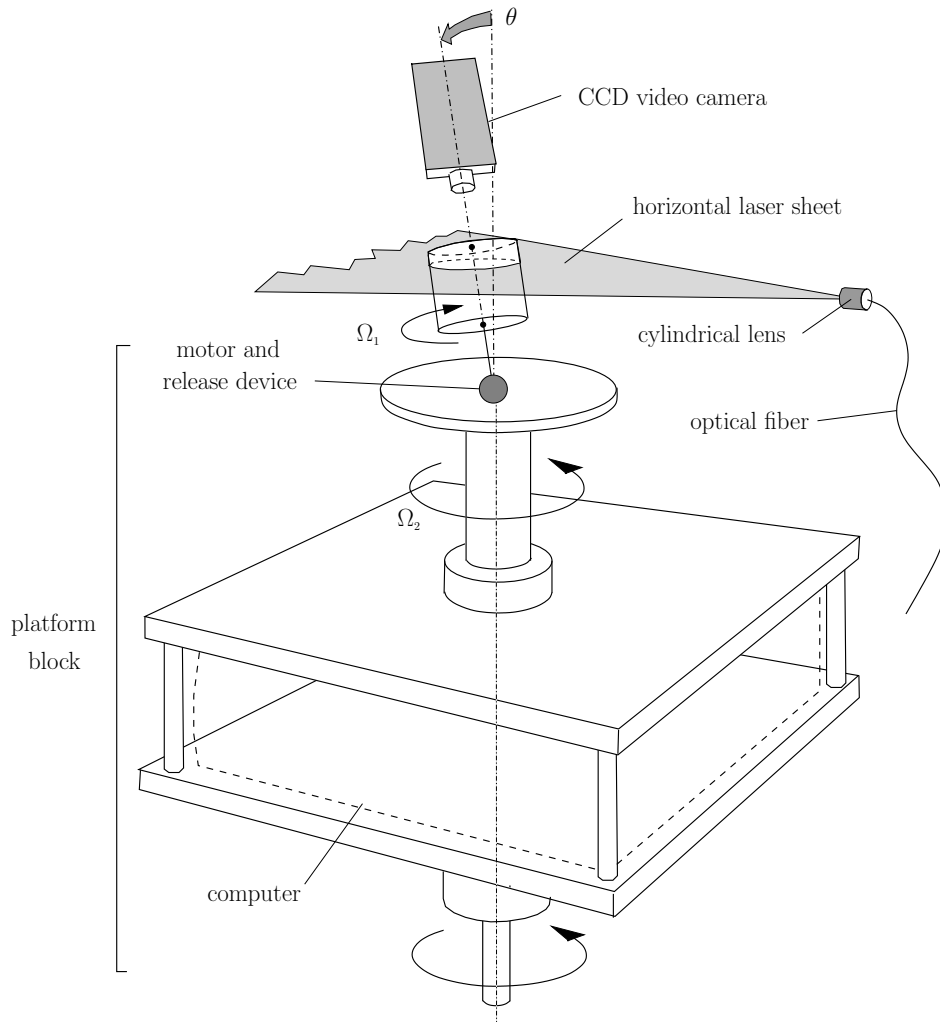
FIGURE 2. Sketch of the experimental setup. The cylinder is directly mounted on the axis of the motor which is located on the rotating platform, and can be tilted during the rotation of the platform. The camera, located above the cylinder is fixed in the platform frame of reference. The whole platform block, including the computer, rotates at angular frequency Ω_2.

(a)   (b)
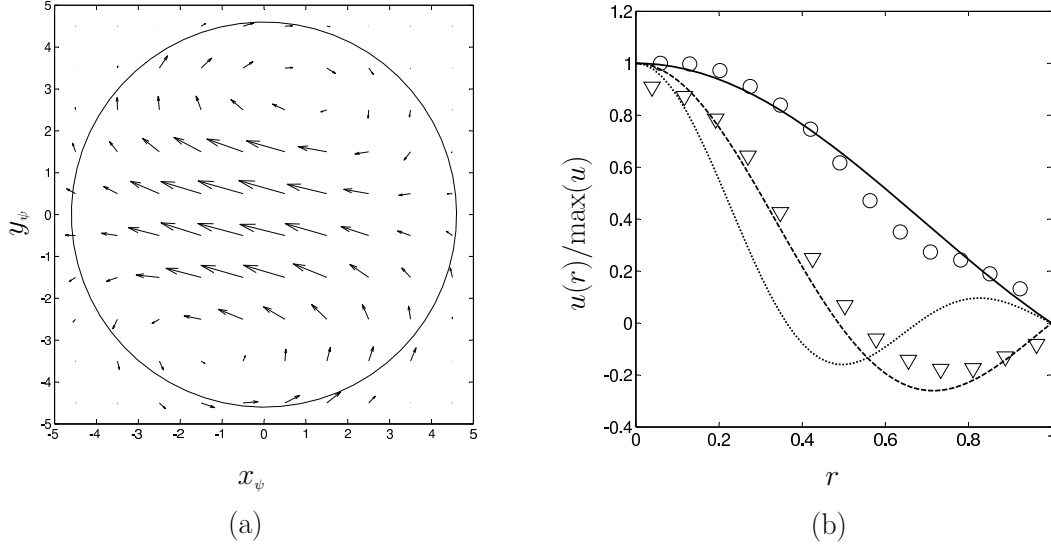
FIGURE 3. (a) Velocity field measured at $\omega = 0.9$, i.e. close to the first resonance $\omega_{1,1} = 0.996$ of mode $i = 1$ ($Re = 5500$, $h = 2$ and $\varepsilon = 1.7 \times 10^{-3}$). (b) radial velocity along the x_ψ-axis. The circles ($\circ$) correspond to the field displayed in (a). The triangles ($\triangledown$) correspond to a velocity field at $\omega = 0.45$ with $\varepsilon = 9.6 \times 10^{-3}$, i.e. close to $\omega_{1,2} = 0.51$. The related linear theoretical profiles are plotted in solid and dashed lines. The dotted line corresponds to the theoretical profile for the third Kelvin mode.
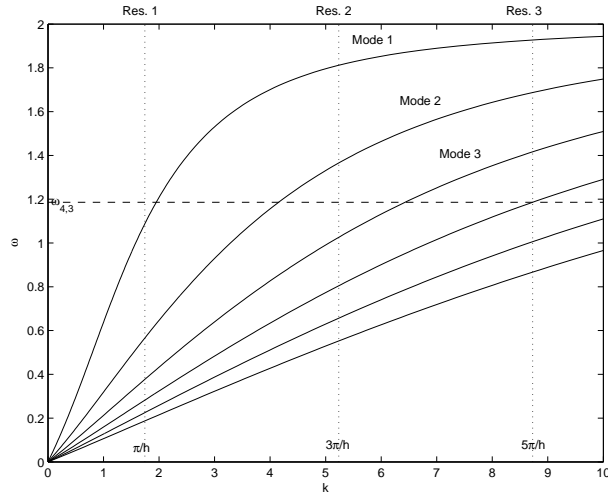
FIGURE 4. Dispersion relation of the Kelvin modes with an azimuthal wavenumber $m = 1$, given by (3.7) and (3.8). The dotted lines correspond to the resonances for an aspect ratio $h = 1.8$.
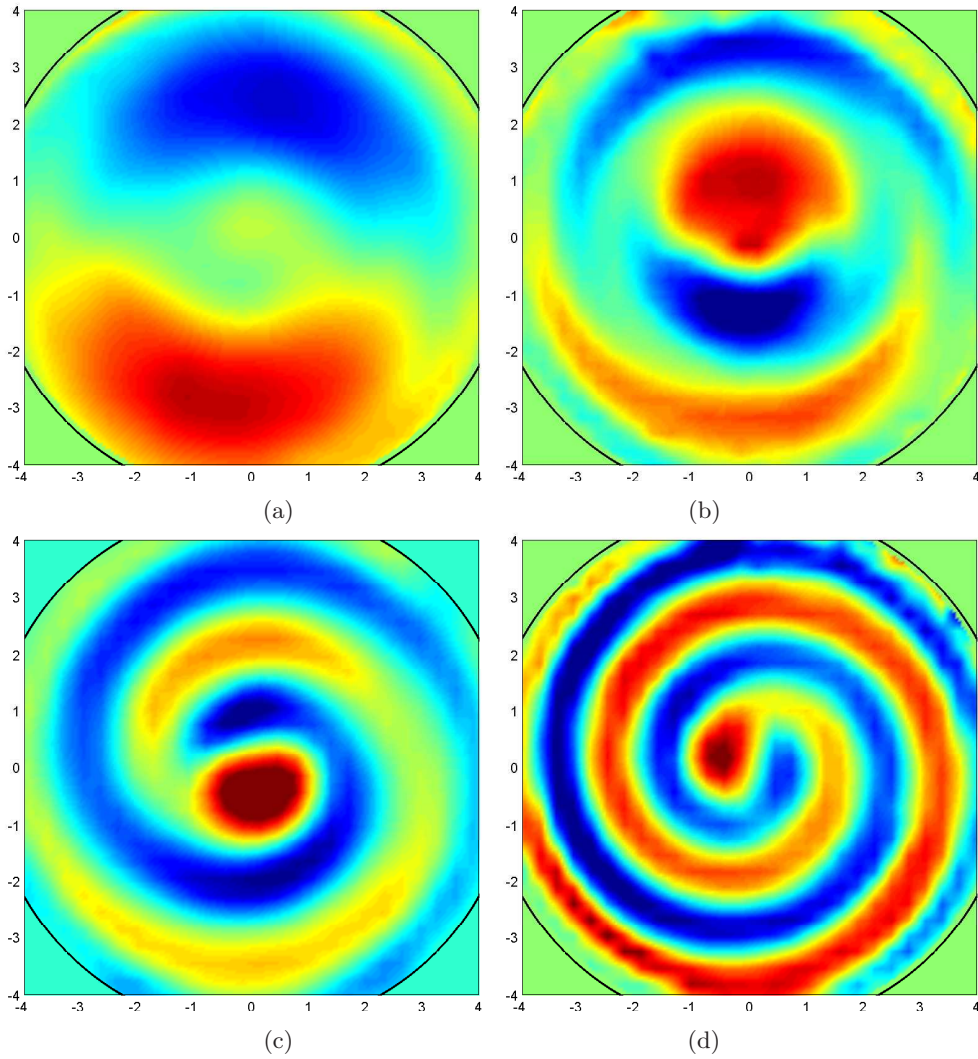
FIGURE 5. Vorticity fields of the first (a), second (b), third (c) and fifth (d) Kelvin mode, observed close to their first resonance (where k_i is close to π/h). Here, $h = 2$ and the flows are observed respectively for $\omega = 0.9, 0.45, 0.3, 0.2$. The Reynolds number is equal to 5500 (a), 11800 (b), 17700 (c) and 26600 (d) and the small parameter ε is equal to 1.7×10^{-3} (a), 9.6×10^{-3} (b), 1.2×10^{-2} (c) and 1.4×10^{-2} (d).
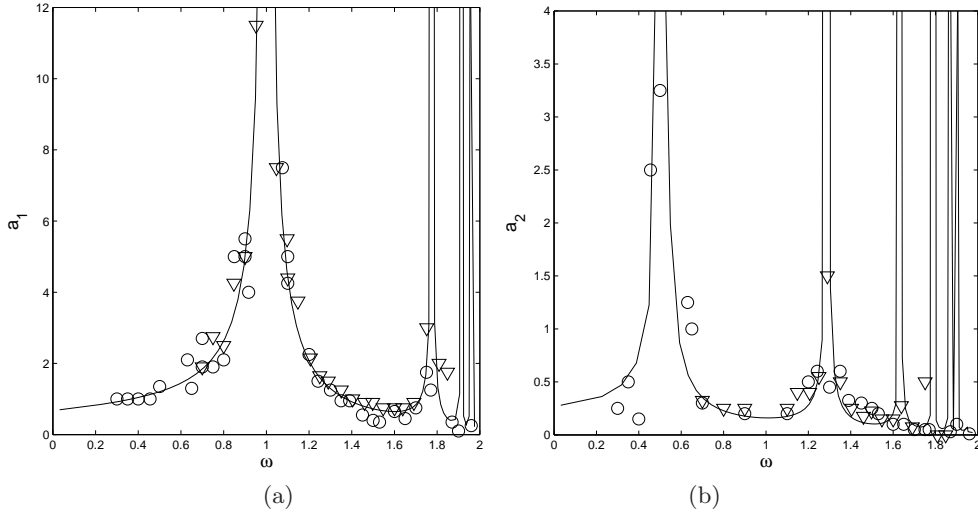
FIGURE 6. Amplitude of the first mode ($i = 1$) (a) and second mode ($i = 2$) (b) for a cylinder of radius $R_c = 4.66$ cm and an aspect ratio $h = 2$. The angular velocity of the cylinder Ω_1 is equal to 2 rad s^{-1} ($\circ$) and 8 rad s^{-1} ($\triangledown$) so that the Reynolds number lies between 2×10^3 and 2×10^5. The solid line shows the prediction of the linear inviscid theory as done in §3.1.
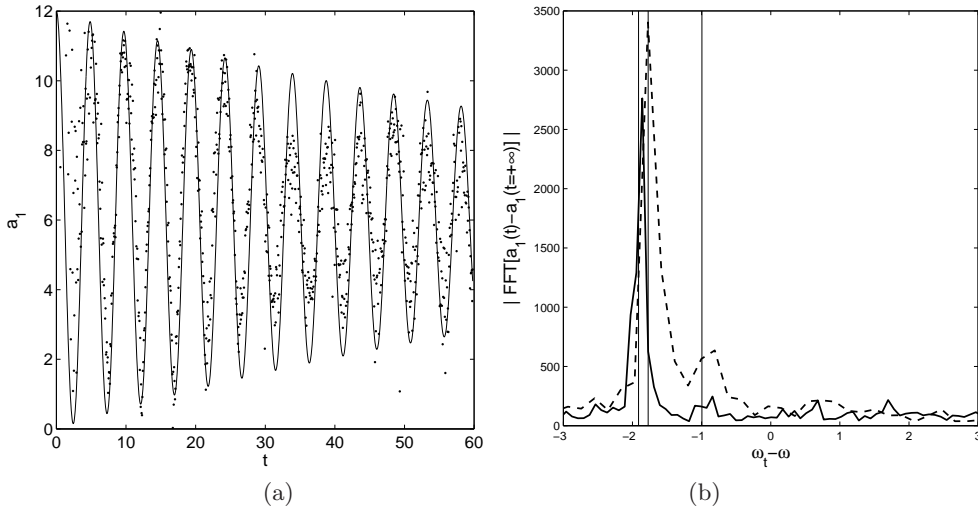
FIGURE 7. (a) Transient dynamics of the first mode amplitude for a forcing frequency $\omega = 0.8$ and a Reynolds number $Re = 6640$. (b) Spectrum of the amplitude for $\omega = 0.8$ (solid line) and $\omega = 1.1$ (dashed line). The corresponding Reynolds numbers are $Re = 6640$ and $Re = 4830$ respectively. The Fourier transform of the temporal signals is plotted as a function of the transient dimensionless frequency $(\Omega_t - \Omega_1)/\Omega$ (given in the cylinder frame). The thin solid lines correspond to the first three resonances of the Kelvin mode $i = 1$: $\omega_{1,1} = 0.996$, $\omega_{1,2} = 1.774$, $\omega_{1,3} = 1.912$. Here, $\varepsilon = 3.5 \times 10^{-3}$ and $h = 2$.
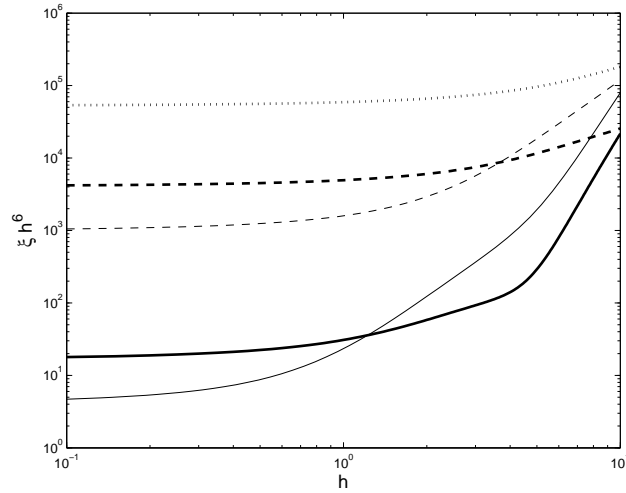
FIGURE 8. Numerical value of the nonlinear parameter ξ multiplied by h^6 quantifying the interaction of the resonant Kelvin mode with the geostrophic mode. The curves correspond to the first (thick lines) and second (thin lines) Kelvin modes at their first (solid line), second (dashed line) and third (dotted line) resonance.
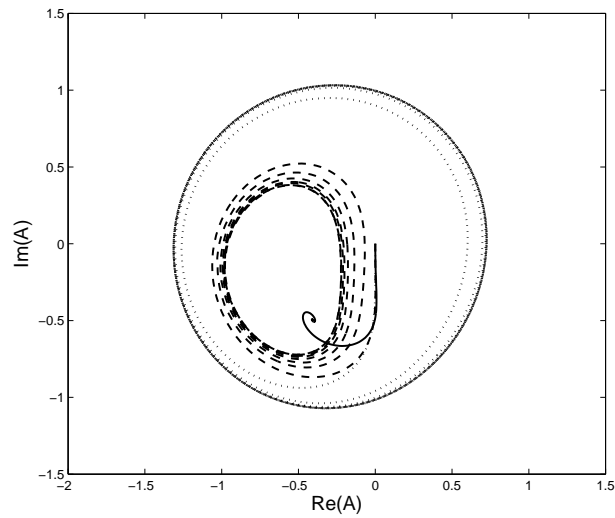
FIGURE 9. Phase portrait of the complex amplitude of the first Kelvin mode at its first resonance, obtained by integrating equations (4.20a,b). The Reynolds number is equal to 2.5×10^4 (solid line), 2.2×10^5 (dashed line) and 2.5×10^6 (dotted line) for a small parameter $\varepsilon = 0.003$ as in the experiments. This corresponds to η equals 0.31, 0.10 and 0.03 respectively.

P. Meunier, C. Eloy, R. Lagrange and F. Nadal
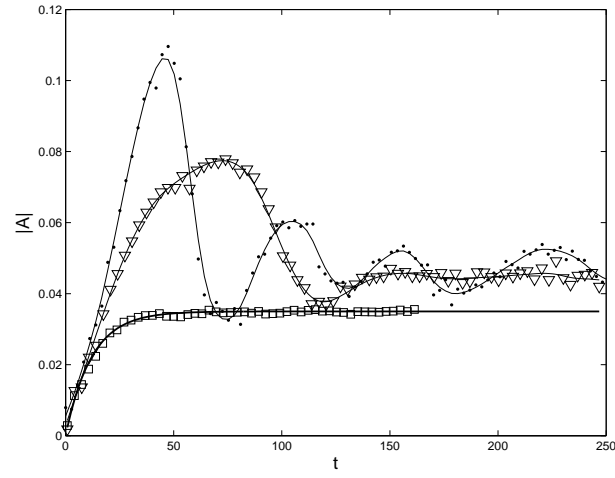
FIGURE 10. Time evolution of the amplitude of the first mode at the second resonance ($\omega = 1.812$ and $h = 1.8$) for $Re = 720$ ($\square$), $Re = 2200$ ($\triangle$) and $Re = 7400$ ($\bullet$). The thick line corresponds to an exponential fit for $Re = 720$. The forcing amplitude is $\varepsilon = 2.8 \times 10^{-3}$.
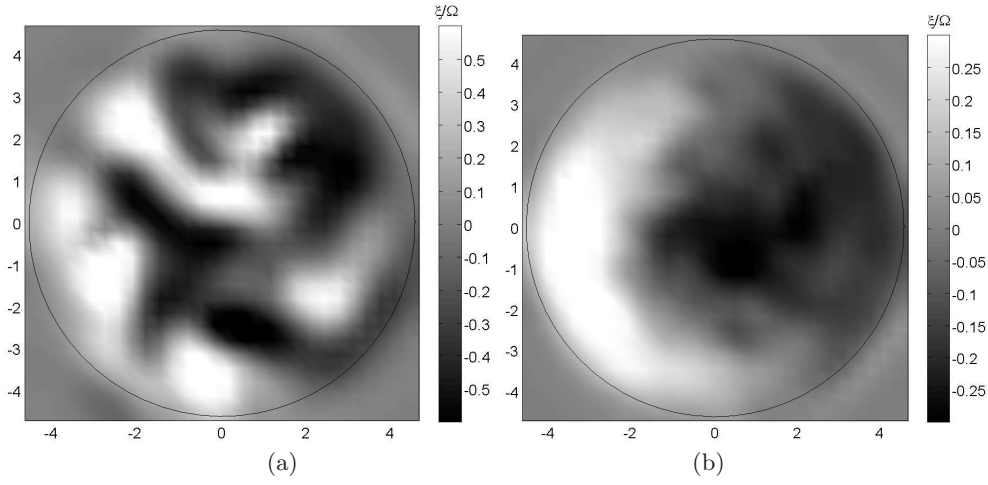
FIGURE 11. Instantaneous (a) and mean (b) vorticity field of the second resonance of the first Kelvin mode ($\omega = 1.812$ and $h = 1.8$) after destabilisation of the flow ($Re = 7400$ and $\varepsilon = 2.8 \times 10^{-3}$).
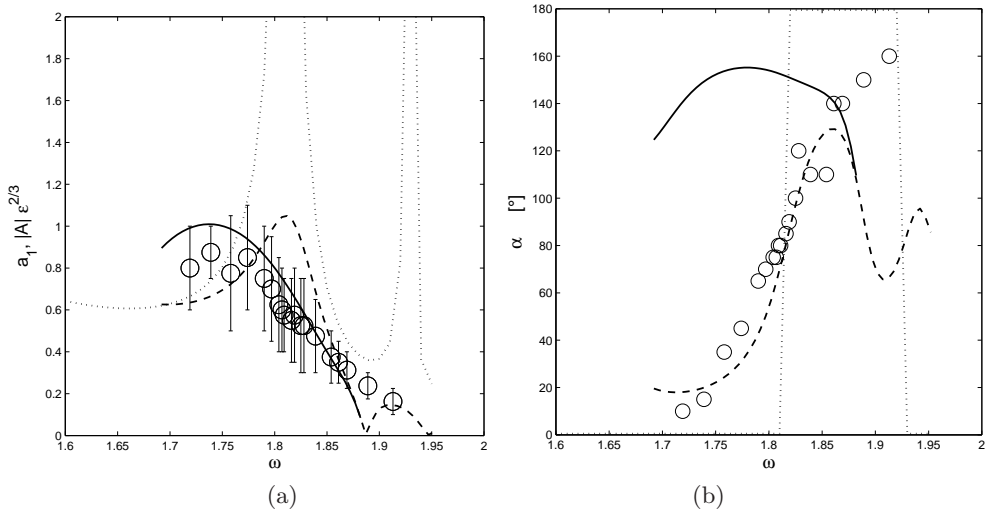
FIGURE 12. Amplitude (a) and orientation (b) of the first Kelvin mode around its second resonance. Experimental results (○) are obtained for an aspect ratio $h = 1.8$, Reynolds number $Re = 2500$ and ε varying between 2.3×10^{-2} and 3.3×10^{-2}. The solid line corresponds to the non linear viscous theory at the second resonance of the first mode, the dashed line to the linear viscous theory and the dotted line to the linear inviscid theory.
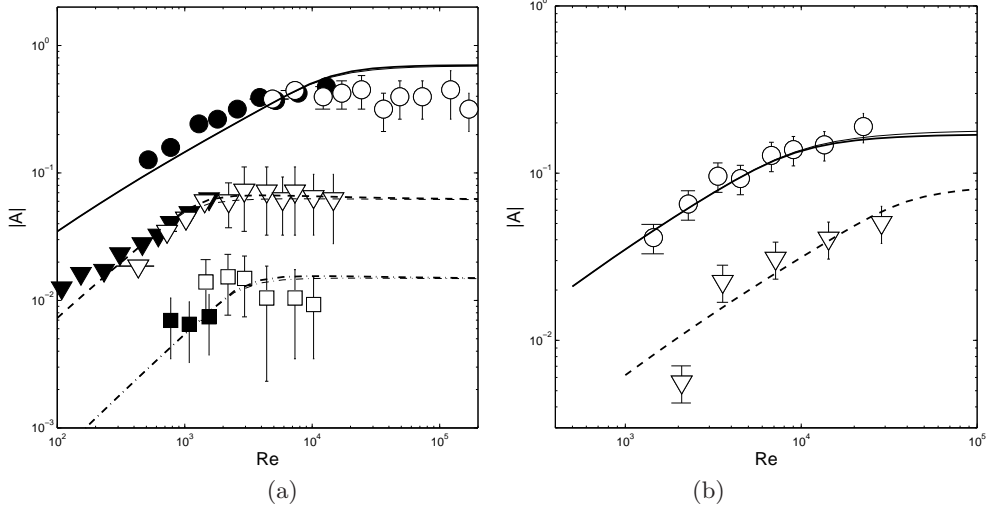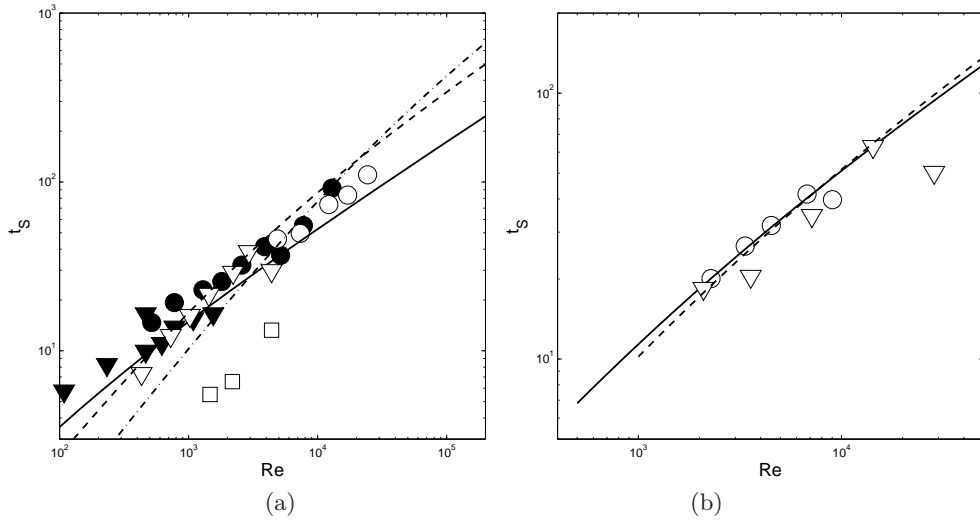
FIGURE 13. Amplitude of the first (a) and second (b) Kelvin modes as a function of the Reynolds number for the first ($\circ$, solid line), second ($\triangledown$, dashed line), and third ($\square$, dash-dotted line) resonances. Closed symbols correspond to a small cylinder $R_c = 1.5$ cm and open symbols to a large cylinder $R_c = 4.6$ cm. The thick lines correspond to the approximate theory (4.20) and the thin lines to the exact theory (4.14) and (4.17). For the first mode, $h = 1.8$; $\varepsilon = 3.1 \times 10^{-3}$, 2.8×10^{-3} and 3.2×10^{-2} for the first, second and third resonance respectively. For the second mode $h = 2$; $\varepsilon = 8.6 \times 10^{-3}$ and $\varepsilon = 5 \times 10^{-3}$ for the first and second resonance respectively.

FIGURE 14. Settling time of the first (a) and second (b) modes as a function of the Reynolds number, obtained at the first (○, solid line), second (▽, dashed line) and third (□, dash-dotted line) resonances. Closed symbols correspond to a small cylinder and open symbols to a large cylinder. Same experimental parameters as in Fig. 13.
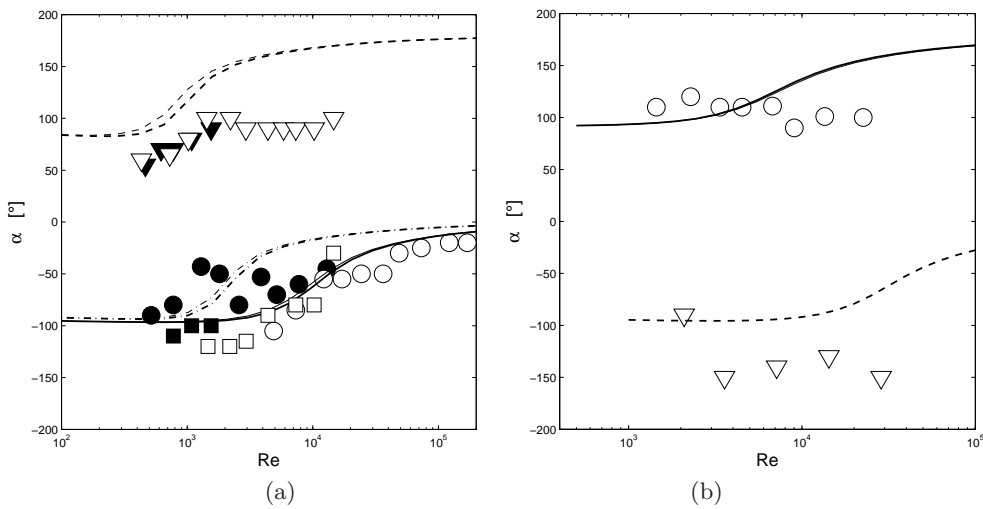

FIGURE 15. Orientation of the first (a) and second (b) modes as function of the Reynolds number, obtained at the first (○, solid line), second (▽, dashed line) and third (□, dash-dotted line) resonances. Closed symbols correspond to a small cylinder and open symbols to a large cylinder. The thick lines corresponds to the approximate theory (4.20) and the thin lines to the exact theory (4.14) and (4.17). Same experimental parameters as in Fig. 13.
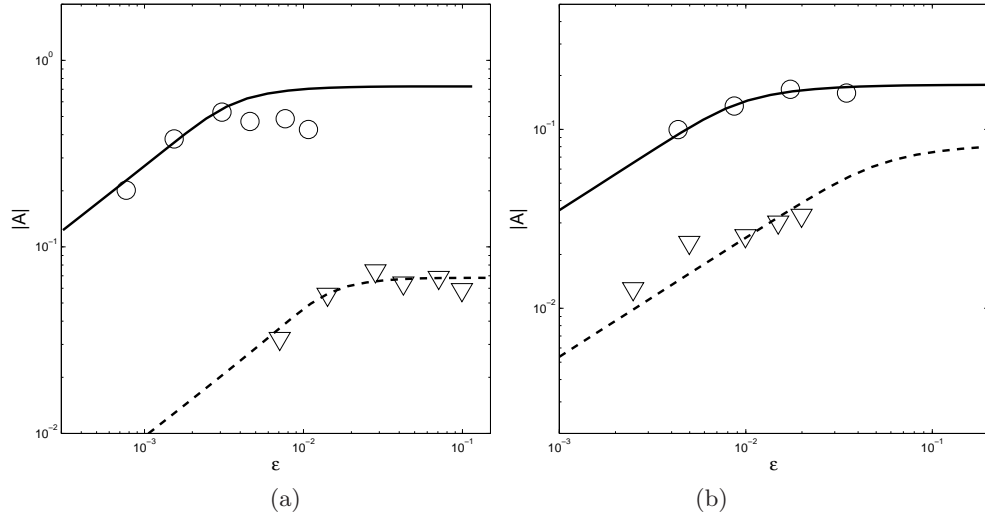
(a)   (b)

FIGURE 16. Amplitudes of the first (a) and second (b) modes as a function of the parameter ε (proportional to the precessing angle θ), obtained at the first ($\circ$, solid line) and second ($\triangledown$, dashed line) resonances. For the first mode, $h = 1.8$ and $Re = 11900$ (resp. 2150) for the first (resp. second) resonance. For the second mode, $h = 2$ and $Re = 9000$ (resp. 3600) for the first (resp. second) resonance.
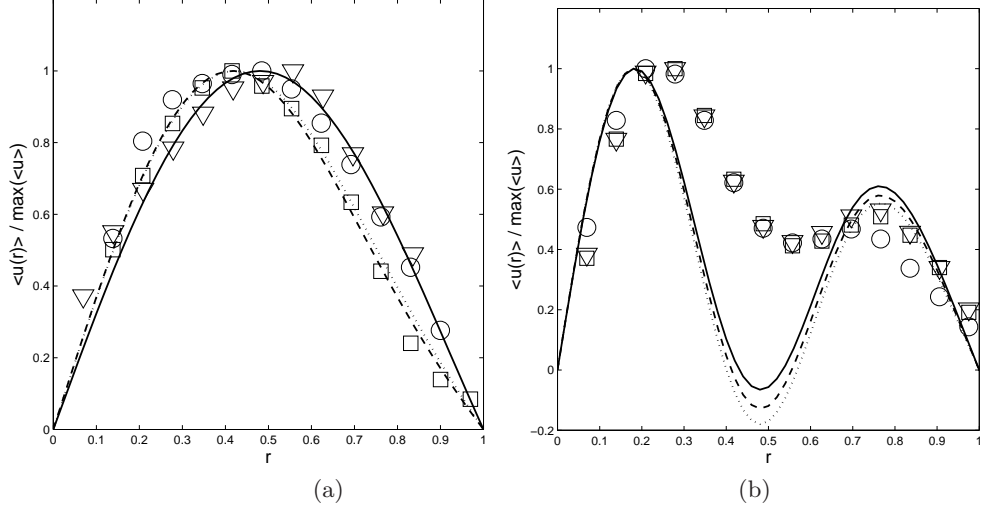
FIGURE 17. Velocity profile of the geostrophic mode ($m = 0$) for the first resonance of (a) the first ($\omega = 1.088$, $h = 1.8$, $\varepsilon = 3.1 \times 10^{-3}$) and (b) the second ($\omega = 0.51$, $h = 2$, $\varepsilon = 8.6 \times 10^{-3}$) Kelvin mode. (a) $Re = 1300$ ($\circ$, solid line), $Re = 4900$ ($\triangledown$, dashed line) and $Re = 12200$, ($\square$, dotted line); (b) $Re = 3900$ ($\circ$, solid line), $Re = 7800$ ($\triangledown$, dashed line) and $Re = 16000$ ($\square$, dotted line).
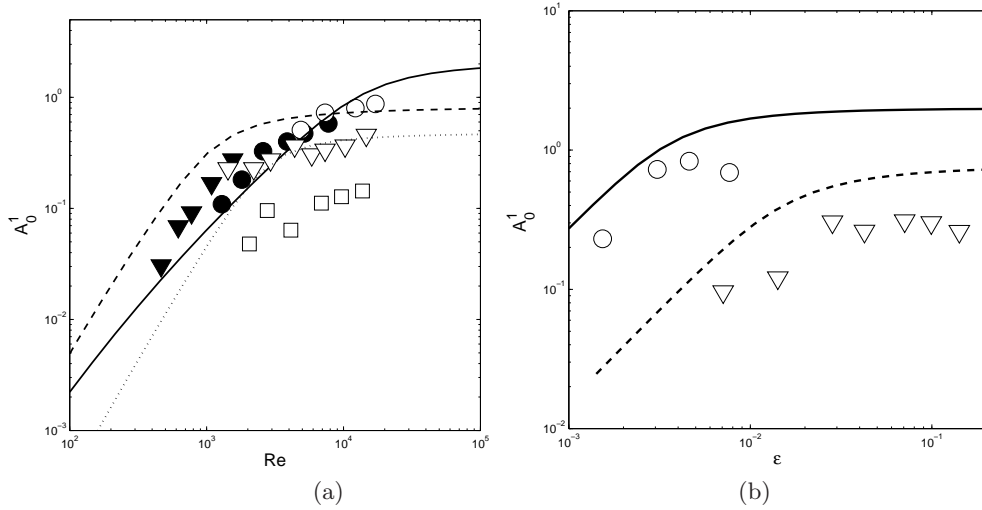

FIGURE 18. Amplitude of the geostrophic mode as a function of the Reynolds number (a) and the precession angle (b). The results are obtained with an aspect ratio $h = 1.8$ for the first mode at its first resonance ($\circ$, solid line, $\omega = 1.088$), its second resonance ($\triangledown$, dashed line, $\omega = 1.812$) and its third resonance ($\square$, dotted line, $\omega = 1.927$). Closed symbols correspond to a small cylinder and open symbols to a large cylinder. (a) $\varepsilon = 3.1 \times 10^{-3}$, 2.8×10^{-3} and 3.2×10^{-2} for the first, second and third resonance respectively.; (b) $Re = 12200$ for the first resonance and $Re = 2200$ for the second resonance.
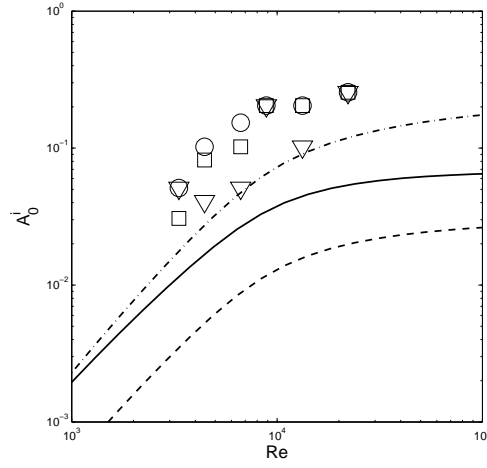
FIGURE 19. Amplitude of the geostrophic mode as a function of the Reynolds number, for the first resonance of the second mode. The different curves correspond to the first component A_0^1 (solid line, $\circ$), the second component A_0^2 (dashed line, $\triangledown$) and the third component A_0^3 (dash-dotted line, $\square$). The dimensionless parameters are $h = 2$, $\varepsilon = 8.6 \times 10^{-3}$.